Establishing benchmarks for quantitative mapping of m^{6}A by Nanopore Direct RNA Sequencing

Authors

Denise Ohnezeit*[1], Elene Loliashvili*[2], Gregory Putzel[3], Ruth Verstraten[2,4], Jianheng Liu[5], Luke S. Nicholson[5], Alejandro Pironti[3], Samie R. Jaffrey[5], Daniel P. Depledge[#1,2,4,6], Angus C. Wilson[#1]

Affiliations

[1]Department of Microbiology, New York University School of Medicine, New York, NY, USA

[2]Institute of Virology, Hannover Medical School, Hannover, Germany

[3]Antimicrobial-Resistant Pathogens Program, New York University Grossman School of Medicine, New York, NY, USA

[4]German Center for Infection Research (DZIF), partner site Hannover-Braunschweig, Hannover, Germany

[5]Department of Pharmacology, Weill Medical College, Cornell University, New York, NY, USA

[6]Cluster of Excellence RESIST (EXC 2155), Hannover Medical School, Carl-Neuberg-Straße 1, 30625 Hannover, Germany

* Joint first authors: contributed equally

[#] Joint senior authors: contributed equally

ORCIDs

DO = 0000-0002-2346-2545

EL = 0009-0006-4098-5010

GP = 0000-0002-5211-2608

RV = 0009-0008-6046-6335

JL = 0000-0003-0216-1951

LSN = 0009-0005-8203-7249

AP= 0000-0002-7759-6776

SRJ = 0000-0003-3615-6958

DPD = 0000-0002-4292-0599

ACW = 0000-0002-5016-4164

Abstract

Nanopore direct RNA sequencing (DRS) coupled with Dorado modification-aware basecalling enables mapping of epitranscriptomic modifications including N^6-methyladenosine (m^6A) at the level of individual RNAs. However, a lack of systematic benchmarking continues to raise questions regarding the sensitivity, specificity, and reproducibility of this method. To address this and to establish a best-practice workflow, we evaluated multiple Dorado versions using *in vitro* transcribed RNA and an m^6A methyltransferase inhibitor as specificity controls. We established that stringent filtering is necessary to reduce false-positive calls and found strong concordance at high-stoichiometry sites when compared to an orthogonal m^6A mapping method (GLORI). Further, by applying DRS to primary human fibroblasts and HD10.6 neurons, we uncovered cell type-specific differences in m^6A stoichiometry, indicating a finely tuned epitranscriptomic regulation. Our study thus presents the first systematic comparison of Dorado and GLORI from the same input RNA and expands characterization of the m^6A epitranscriptome to fibroblasts and neurons.

Introduction

Epitranscriptomics describes the occurrence of chemical modifications on RNA that regulate stability, localization, splicing, translation or decay[1]. To date, over 170 RNA modifications are known to occur across all classes of RNA including eukaryotic mRNA[2]. Of these, at least thirteen different chemical modifications have been characterized in mRNAs, comprising both cap-proximal and internal modifications[3]. By contrast, current evidence indicates that lncRNAs harbor a more limited repertoire of modifications, primarily N^6-methyladenosine (m^6A), 5-methylcytosine (m^5C), and N7-methylguanosine (m^7G)[4]. One of the best studied and most abundant internal mRNA modifications is m^6A. Functional studies of m^6A methylases, demethylases and m^6A binding proteins, as well as sequencing-based mapping methods have increased our understanding of m^6A as a reversible and dynamic modification that fine-tunes nearly all aspects of mRNA metabolism[5-9].

In addition to m^6A, other widespread and functionally important marks include m^5C, which is less abundant but influences mRNA export and stability, pseudouridine (Ψ), which contributes to mRNA stability, translation and splicing, and adenosine-to-inosine (A to I) editing, which is involved in splicing, stability and recoding events that contribute to protein diversity[10].

Techniques based on short-read (Illumina) sequencing have advanced in recent years to achieve single-nucleotide resolution and quantitative mapping of RNA modifications. The approaches that have emerged

59 to map m^6A can be broadly classified as antibody-based, enzyme-assisted or chemical conversion
60 methods[11].

61 Early antibody-based techniques[12-14] provided the first transcriptome-wide insights into m^6A architecture,
62 albeit at limited resolution. Enzyme-assisted methods[15,16] have improved precision but can introduce
63 enzymatic biases. These biases are avoided with GLORI-Sequencing (GLORI), which selectively deaminates
64 unmethylated adenosines, enabling theoretically unbiased, quantitative, single-nucleotide mapping of
65 m^6A[17].

66 Despite advances, the broad utility of these approaches is limited by a lack of isoform specificity, as well
67 as biases associated with amplification, specificity of antibodies or variable adenosine conversion rates[18].
68 Oxford Nanopore Technologies (ONT) direct RNA sequencing (DRS) offers an alternative to these methods
69 by analyzing native RNA molecules that have retained their modifications[19]. As single RNAs pass through
70 nanopores, signal changes are interpreted to determine canonical and modified residues at single-
71 nucleotide resolution on individual transcripts[20,21]. For the now discontinued DRS SQK-RNA002 chemistry
72 used with R9 flowcells, multiple research groups developed algorithms for detecting RNA modifications.
73 These methods can be divided into error rate-based and current signal-based[22]. While the recent release
74 of the DRS SQK-RNA004 chemistry and RNA-specific flowcells reduced the utility of many of these tools,
75 introduction of a modification-aware basecaller (Dorado) provides an all-in-one toolkit for basecalling,
76 RNA modification detection, and poly(A) tail length estimation. Early versions of Dorado (e.g. v0.5.0 and
77 v0.6.0) enabled m^6A (DRACH-context only) detection, while version v0.7.0 enabled detection of Ψ and all-
78 context m^6A. More recent versions (v0.8.0 and v0.9.0) allow both DRACH- and all-context m^6A detection,
79 together with Ψ, inosine and m^5C[23].

80 In a recent overview of this emerging technology, Cruciani and Novoa highlighted the importance of
81 rigorous evaluation of the limitations of Dorado and advocated forcefully for the establishment of best
82 practices to ensure consistency and accuracy going forward[24]. To date, only a handful of studies of this
83 kind have been published. A series of studies from Novoa and colleagues showed that Dorado performs
84 robustly on synthetic modified and unmodified RNA molecules but also found that overlaps in the
85 identification of specific modifications and false-positive calls remain a challenge but can be mitigated by
86 the inclusion of *in vitro* transcribed (IVT) controls[25,26]. Independently, Esfahani and colleagues used poly(A)
87 RNA from a B-lymphocyte cell line to compare SQK-RNA002 and SQK-RNA004-derived DRS data. While
88 they concluded that Dorado outperformed other RNA modification detection tools, IVT controls were
89 necessary to reduce false-positive calls[27]. Recent benchmarking efforts comparing Dorado and m6Anet on

SQK-RNA004 chemistry have shown that both tools achieve high recall and strong stoichiometry correlations at DRACH motifs but exhibit higher false discovery rates on IVT controls and lower recalls of low-stoichiometry genomic m^6A sites. However, these evaluations relied on previously published GLORI and eTAM-Seq datasets, rather than matched input material[23,26]. By directly comparing m^6A detection by DRS coupled with Dorado and GLORI on the same RNA inputs, our study overcomes this limitation. Specifically, we systemically benchmark multiple versions of Dorado using poly(A) RNA from primary (normal) human dermal fibroblasts (NHDFs) and functional human neurons produced through terminal differentiation of HD10.6 cells[28], along with IVT RNA. We included treatments with STM2457, an enzymatic inhibitor of the primary m^6A methyltransferase METTL3[29], to robustly assess false-positive m^6A detection rates and also compared the DRS outputs with those obtained from GLORI[30] using the same RNA as input. While our analysis is centered on the sensitivity and specificity of m^6A detection in DRS datasets, we also benchmark the ability of Dorado to reliably detect m^5C, Ψ, and inosine. Together, our data provides a robust workflow for DRS-based modification detection that reliably captures transcriptome-wide, isoform-level, site-specific stoichiometries of RNA modifications.

Results

Systematic benchmarking of ONT's Dorado across human cell types.

To evaluate the performance of ONT's basecalling tool Dorado across different human cell types, we selected primary NHDFs and differentiated HD10.6 cells as a neuron-like model. Prior to isolation of total RNA, cells were treated for 48h with a small molecule inhibitor of METTL3 (STM2457) or with vehicle (DMSO). We then isolated poly(A) RNA and subjected the same input material to both DRS and GLORI. The same material was also used to generate IVT RNA (**Fig. 1A**). Dorado basecalling using version v.0.9.0 resulted in over 13M reads using poly(A) RNA from NHDFs treated with DMSO or STM2457, while we obtained over 5M and 10M reads from DMSO- and STM2457-treated HD10.6 cells, respectively. The rate of primary alignment to the human genome (hg38) was over 98% for all the sequenced samples. A detailed overview of read statistics generated by DRS can be found in **Supplementary Table S1**.

To systematically benchmark Dorado, we performed basecalling using versions v0.5.0 through v0.9.0. Reads were aligned to the human genome and transcriptome to obtain comprehensive information on

119 isoform-level modification detection. Further, we explored different aspects of detected modifications
120 using the outputs generated by ONT's Modkit tool[31]. We assessed multiple filtering strategies using base
121 and modification probabilities, as well as stoichiometry distributions, and evaluated them based on the
122 IVT data and sensitivity to METTL3 inhibition. By filtering out false-positive calls using multiple control
123 layers, we determined high-confidence m^6A sites (**Fig. 1B**). Finally, we compared these high-confidence
124 predictions with sites identified by GLORI performed on the same input RNA. Using these results, we
125 developed a benchmarked pipeline that filters m^6A sites predicted by Dorado to minimize false-positive
126 detection without impacting sensitivity (**Fig. 1C**).

127

128 **Stringent filtering of modification probabilities removes false positives**

129 During modification-aware basecalling, each nucleotide is assigned a basecall probability score ranging
130 from 0 to 1. Similarly, individual modified nucleotides are assigned a modification probability score in the
131 same range. To establish a baseline for false-positive m^6A predictions, we plotted basecall and modification
132 probability distributions for an IVT poly(A) RNA dataset processed using Dorado v0.9.0 and aligned to
133 human genome (**Fig.2**). We binned basecall and modification probability values for A and m^6A (all-context
134 and DRACH) and compared this data from DMSO- and STM2457-treated NHDF datasets.

135 We observed that 75-90% of A basecalls (in all datasets) have probability scores above 0.8 **(Fig. S1A)**. Since
136 all A bases are considered during all-context m^6A calling, the fraction of m^6A sites is substantially smaller
137 when compared to DRACH-context m^6A sites (**Fig.2A,B, Fig.S1B,C**). The modification probability
138 distributions are effectively identical for DMSO-treated, STM2457-treated and IVT datasets below 0.98,
139 while the profiles differ substantially at probabilities ≥ 0.98. This suggests that sites detected below 0.98
140 are likely false positives, indicating that only high-probability m^6A calls can be considered reliable. Here,
141 STM2457 treatment shows a marked reduction in the number of reported m^6A sites in both all-context
142 and DRACH-only datasets when compared to the DMSO treatment (**Fig. 2A,B**).

143 In addition to m^6A, we examined modification probability distributions for Ψ, inosine and m^5C, each of
144 which can be basecalled with Dorado v0.9.0 (**Fig. S2**). For Ψ and I, the modification probability distributions
145 for the STM2457 and DMSO datasets only diverge from the IVT dataset at ≥ 0.99 modification probability,
146 thus providing a relevant threshold for filtering out false positives (**Fig. S2A,B**). By contrast, m^5C
147 modification probability distributions were similar between all three datasets and no filter could be

148 adequately established (**Fig. S2C**). While this likely reflects a low rate of m^5C installation, it also indicates
149 that the m^5C model utilized by Dorado requires further refinement.

150 Modification probability distributions have similar profiles for transcriptome-aligned NHDF data (**Fig. S3)**
151 as well as genome- and transcriptome-aligned data from HD10.6 cells **(Fig. S4, Fig. S5**). Of note, the fraction
152 of high-probability inosine sites is increased in STM2457-treated cells, compared to DMSO-treated ones
153 in genome-aligned data (**Fig. S2B, Fig.S4D**), which points to increased numbers of retained introns in the
154 METTL3-inhibited sample. Accordingly, this effect is absent in transcriptome-aligned data (**Fig. S3D, Fig.**
155 **S5D**).

156 While IVT transcriptomes serve as excellent negative controls, we also considered whether the RNA
157 calibration strand (RCS) that is added during DRS library preparation could serve a similar function. The
158 RCS is a synthetic Enolase II RNA derived by IVT[13] that, similarly to the IVT transcriptomes, are devoid of
159 RNA modifications. Despite the reduced diversity of sequence in the RCS data, the overall results were
160 comparable to that from the IVT transcriptome data (**Fig. S6A,B, Fig. 2A,B**), demonstrating that the RCS
161 can be used as a "built-in" negative control for modification detection with DRS. Finally, we determined
162 that basecall and modification probability distributions remain generally consistent between Dorado
163 versions although more m^6A and Ψ sites are detected with high modification probability in Dorado versions
164 v0.8.0/v0.9.0 compared to v0.7.0 (**Fig. S6C-E)**.

165 **Filtering by stoichiometry further eliminates potential false positives**

166 We next examined the stoichiometry distributions for all m^6A sites in both unfiltered and filtered NHDF
167 datasets (**Fig. S7**). Here, unfiltered datasets showed that the vast majority of m^6A sites, 92% for all-context
168 and 75% for DRACH-context, have stoichiometry values < 10% with less than 1% sites showing high (> 50%)
169 stoichiometry. Application of our filtering strategy removed over 70% of the sites (**Fig. 2E)**, regardless of
170 the context, almost all of which showed stoichiometries of < 10%, without significantly changing the
171 numbers of high stoichiometry sites detected (**Fig. S7**). A similar analysis of the IVT transcriptome revealed
172 large numbers of false positive m^6A sites with stoichiometry values below 10%, most of which were
173 eliminated by application of our filters (**Fig. S8A,B**). However, the remaining presence of low stoichiometry
174 false-positive sites indicates that an additional layer of filtering to exclude sites with < 10% stoichiometry
175 is beneficial. An additional argument in support of our filtering strategy is the observation that treatment
176 with the METTL3 specific inhibitor STM2457 dramatically reduced m^6A installation at sites with ≥ 10%
177 stoichiometry in untreated datasets in a context-independent manner (**Fig. 2C,D, Table S2**). Similar results

178 were observed for the transcriptome-aligned NHDF and HD10.6 m^6A stoichiometry distributions as well
179 (**Fig. S9, Fig. S10, Table S2**).

180 To determine whether our filtering strategy could be applied to other RNA modifications detected by
181 Dorado, we generated stoichiometry distributions for Ψ and inosine in unfiltered and filtered (≥ 0.99
182 modification probability) human genome-aligned DMSO- and STM2457-treated NHDFs and HD10.6s. As
183 with m^6A (**Fig. S7**), 92% of detected Ψ and 96% of inosine have less than 10% stoichiometry (**Fig. S11, Fig.**
184 **S12)**. A recent study that explores Ψ in human mRNAs using 2-bromoacrylamide-assisted cyclization
185 sequencing (BACS) corroborates our results, showing that 82% of Ψ modifications are detected at low
186 levels (below 20%)[32].

187 Above 10% stoichiometry, in our data, there are more inosine sites in STM2457-treated cells than
188 DMSO-treated cells, reflected also in the stoichiometry distributions (**Fig. S11, Fig. S12, Table S2**). Ψ and
189 inosine stoichiometry distributions in our IVT data **(Fig.S8C,D)** further validates our filtering strategy of ≥
190 0.99 modification probability, as it substantially reduces the number of detected false-positive sites in the
191 unfiltered data even at higher (> 50%) stoichiometries in case of inosine (**Fig.S8D**).

192 We have thus demonstrated that setting thresholds for basecall modification probabilities provides a
193 robust method for identifying and filtering false-positive modification calls. For the purposes of this study,
194 we further evaluated the effect of placing the modification threshold on the modification data and
195 restricted the downstream analyses to m^6A sites with probability scores ≥ 0.98.

196

197 **RNA modification detection rates differ between Dorado versions**

198 Dorado basecalling relies on models generated using Remora (github.com/nanoporetech/remora) that are
199 frequently updated. This raises an important question as to whether these updates produce notably
200 different outputs that could impact biological interpretation. To address this, we utilized multiple Dorado
201 versions and Remora models to perform modification calling of our NHDF dataset. We restricted our
202 analyses to m^6A and Ψ as these are the only modifications that could be detected in previous versions.
203 Here, we observe that m^6A and Ψ stoichiometry distributions are generally consistent between different
204 Dorado versions (**Fig. S13**), albeit with greater numbers of low stoichiometry (< 10%) sites detected in
205 older Dorado versions. There is a large overlap of the detected ≥ 10%-stoichiometry m^6A (DRACH and all-
206 context) and Ψ sites between versions, although there are a lot of unique all-context m^6A and Ψ sites
207 identified with just v0.7.0 and not v0.8.0-v0.9.0, that are reduced after applying our modification

208 probability filter (**Fig. S14A,B**). Ψ sites uniquely detected with different versions are found in slightly
209 different sequence contexts (**Fig. S14C,D**). Thus, while RNA modification detection with Dorado is sensitive
210 to changes in the underlying models/versions, this can be effectively controlled through the application of
211 filters that only retain sites with high-confidence modification probability calls.

212

213 **GLORI exhibits reduced specificity but converges with Dorado predictions at high stoichiometry sites**

214 To assess the agreement of DRS Dorado-derived predictions with an orthogonal m^6A detection method,
215 we conducted GLORI on the same NHDF RNA preparations. To ensure a fair comparison of m^6A sites across
216 the two methods, we applied the following filtering strategies: For Dorado (DRACH model), this included
217 thresholds on modification probability (A ≥ 0.8, m^6A ≥ 0.98) and read coverage (≥ 20). For GLORI, we used
218 filters based on coverage (≥ 20) and statistical significance (p-value ≤ 0.05). Next, we extracted m^6A sites
219 that were present in both DMSO and STM2457 treated samples and removed all sites with ≤ 10%
220 stoichiometry in DMSO (**Fig. 3A**). This stepwise strategy reduced false positives and enabled a fair
221 comparison of the high confidence m^6A sites identified by both approaches.

222 As shown in the violin plots, both the all-context and DRACH-context Dorado models identify similar
223 numbers of m^6A sites (81,012 (all-context model) and 72,372 (DRACH model)), the stoichiometries of
224 which were strongly reduced upon STM2457 treatment (**Fig. 3B**). When we analyzed the motifs of the m^6A
225 sites detected with the all-context model, we observed nearly 9,000 sites outside of DRACH motifs.
226 Importantly, the total number of m^6A sites within DRACH motifs was nearly identical to the number of m^6A
227 sites reported using the DRACH model (**Fig.3B**). Unexpectedly, GLORI detects a substantially higher
228 number of sites when using all motifs (140,934) compared to DRACH motifs alone (27,926) (**Fig. 3C**). The
229 fact that most GLORI-identified sites fall outside DRACH motifs suggests these are false positives. This
230 interpretation is reinforced by the observation that the overlap between Dorado and GLORI datasets
231 remains virtually unchanged when comparing GLORI "all motif" and "DRACH motifs" (n=13,614) site sets,
232 underscoring that the additional non-DRACH sites in GLORI (n= 113,008) are largely spurious (**Fig. S17A**).

233 We obtained similar results when comparing m^6A sites obtained with Dorado and GLORI from HD10.6
234 cells. Overall, we detected a similar number of m^6A sites in HD10.6 cells using the all-context and DRACH-
235 specific Dorado models (77,728 and 67,222, respectively) (**Fig. S17B**). By contrast, we detected 174,282 vs
236 27,965 m^6A sites using GLORI without or with DRACH filtering, respectively (**Fig. S17C**).

237 To evaluate how stoichiometry threshold affects the agreement between GLORI and Dorado, we compared
238 the overlap of high-confidence GLORI-identified sites with Dorado m^6A (DRACH context) calls across
239 increasing m^6A stoichiometry cutoffs (**Fig. 3D**). At the lowest stoichiometry threshold applied (≥ 10%),
240 13,614 sites overlapped, representing less than half (48.8%) of GLORI sites. However, as the stringency
241 increased, the relative overlap increased sharply: at ≥ 20%, nearly 70% of GLORI sites overlapped (11,536
242 sites), at ≥ 50% almost 90% overlapped (6,307 sites), and at the highest cutoff (≥ 80%), over 93% of GLORI
243 sites (3,119 sites) were also detected by Dorado. These results demonstrate that while GLORI detects a
244 broad set of potential m^6A sites, only the sites with high stoichiometries overlap with Dorado, indicating
245 high signal to noise ratios in the GLORI datasets.

246 GLORI relies on the high-efficiency conversion of adenosine to inosine with overall gene A to I conversion
247 rates needing to exceed 95-98%[32,33]. Similarly, we observed the conversion rates for our NHDF and HD10.6
248 dates to be 95% (**Table S3**), but we found that small variations in gene conversion rates can strongly
249 influence the sensitivity and specificity of GLORI, as only high-stoichiometry m^6A sites overlapped with
250 DRS-derived predictions (**Fig. 3D**).

251

252 **DRS coupled with Dorado outperforms GLORI in isoform-specific m^6A detection**

253 Next, we wanted to highlight the advantage of long-read sequencing in terms of mapping reads with
254 isoform-precision to the human transcriptome, which is not possible using GLORI due to its reliance on
255 short-read sequencing. We first confirmed that mapping Dorado-basecalled sites to the human
256 transcriptome results in the detection of similar numbers of m^6A sites in both NHDFs and HD10.6 cells (**Fig.**
257 **S17D,E**). To assess if DRS coupled with Dorado identifies distinct m^6A profiles on different transcript
258 isoforms, we analyzed the *SPEN* gene locus which was previously shown to contain more than 100 m^6A
259 sites[17]. On a genomic level, we detected 42 m^6A sites using DRS, while GLORI only detected 5 m^6A sites
260 (**Fig. 3E**). Out of the 7 total isoforms of *SPEN*, *SPEN-201* and *SPEN-202* were detectable in DRS-derived
261 data, considering a minimal coverage of 20 (**Table S4**). When plotting the m^6A sites detected by
262 transcriptome-aligned DRS data, we found that the *SPEN-201* isoform exhibited more m^6A sites with a
263 higher median stoichiometry compared to the *SPEN-202* isoform (**Fig. 3F**). This example highlights that
264 DRS is superior compared with GLORI for isoform-level m^6A quantification.

265

266 **Dorado profiling reveals cell type differences in m^6A distribution and stoichiometry**

267 To assess the reproducibility of Dorado across DRS datasets derived from different cell types, we compared
268 the m^{6}A methylomes of NHDFs and HD10.6 cells. To ensure a fair comparison, we extracted genes that
269 were expressed in both cell types. Next, we compared the total numbers of high confidence m^{6}A sites in
270 NHDFs and HD10.6 cells within the genes expressed in both cell types and found that 87% of HD10.6-
271 derived m^{6}A sites overlap with those detected in NHDFs (**Fig. 4A**). Site-specific m^{6}A stoichiometries from
272 the shared gene set correlated strongly across cell types (Pearson r = 0.93), although we observed a global
273 shift in the HD10.6 dataset, where m^{6}A stoichiometries were generally higher than in NHDFs (**Fig. 4B**).
274 Gene Ontology (GO) term analysis of genes containing shared or unique m^{6}A sites across NHDFs and
275 HD10.6 cells further revealed that these modifications are enriched in transcripts involved in fundamental
276 cellular processes such as transcriptional regulation, DNA repair, chromatin remodeling, and protein
277 transport suggesting that conserved sites maintain core cellular functions (**Fig. 4C**).

278 We next aimed to conduct a comparative motif analysis of m^{6}A sites detected in NHDFs and HD10.6 cells.
279 Sequence logos confirmed strong enrichment of the canonical DRACH consensus motif for both cell types
280 in modification probability-filtered data, with the GGACU pentamer being the most prominent (**Fig. 4D,E,**
281 **Fig.S15**). Quantification of 5-mer distributions revealed highly similar motif preferences across datasets.
282 While the global motif architecture of m^{6}A deposition is conserved between NHDFs and HD10.6 cells, we
283 observed a trend toward higher stoichiometries in the HD10.6 dataset, particularly within the most
284 abundant DRACH motifs, suggesting enhanced modification efficiency in the neuronal-like context (**Fig. 4F,**
285 **G**).

286 Metagene analysis showed, as known previously, that m^{6}A is enriched near the stop codons and in the 3'
287 UTRs (**Fig. 2F**). Since there have been several studies done on how exon architecture regulates m^{6}A
288 distribution on mRNAs[1,2,3], we also examined m^{6}A sites in monoexonic transcripts separately and observed
289 that monoexonic transcripts are more equally m^{6}A-modified across entire CDS (**Fig. 2F**). m^{6}A (both all-
290 context and DRACH-context) distribution profiles look less typical for all-stoichiometry or < 10%
291 stoichiometry sites in both NHDF and HD10.6 datasets (**Fig. S16**). For all-context m^{6}A (**Fig. S16A**),
292 modification filter also proves to be deciding for the distribution profile, together with ≥ 10%
293 stoichiometry.

294 To connect shared m^{6}A sites with their functional context and illustrate their distribution on individual
295 transcripts, we conducted a KEGG pathway analysis with the genes that contain shared m^{6}A sites between
296 NHDFs and HD10.6 cells. We observed a significant enrichment in pathways related to neurodegeneration,
297 infection, and intracellular signaling, including axon guidance and mTOR signaling (**Fig. 4H**). To further

298 illustrate these findings, we examined representative genes contained in one or more of these pathways.
299 *WNTB5*, *MAPK1*, *AKT1*, *NCK1* and *NRP1* all showed robust methylation in both NHDFs and HD10.6 cells,
300 with consistently higher stoichiometries observed in the neuronal-like context. In contrast, *ACTG1*,
301 included as a housekeeping control not represented in the enriched pathways, displayed stable and
302 comparatively uniform methylation across both cell types (**Fig. 4I**).

303 Together, these results demonstrate that while the global architecture of m^6A deposition is largely
304 conserved between primary fibroblasts and neuronal-like cells, the neuronal context is characterized by a
305 global shift toward higher m^6A stoichiometries, which is readily detectable in single genes. These findings
306 suggest that cell type-specific regulation of m^6A may fine-tune core cellular pathways relevant to that cell
307 type.

308

309 ## Discussion

310 High rates of false positives remain a major problem in epitranscriptomics, even with the advent of
311 modification-aware tolls[24]. Comparing the outputs of orthogonal methods performed on the same input
312 material, combined with use of IVT RNA and/or specific methyltransferase inhibition, offers an effective
313 mitigation strategy[24,26]. The results presented here establish a robust framework that minimizes false
314 positives and enables isoform-specific and quantitative m^6A mapping. Through a direct comparison with
315 GLORI, we showed that combining nanopore DRS datasets with Dorado modification-aware basecalling
316 provides greater scalability, isoform resolution, and reproducibility across different cell types. Further, the
317 simplicity of nanopore DRS library preparation enhances consistency whereas GLORI is constrained by a
318 laborious and technically challenging protocol that is extremely sensitive to adenosine conversion rates[34].
319 Despite these limitations, we determined that the majority of m^6A sites in our filtered DRS datasets could
320 be confirmed by GLORI. By expanding our analysis across multiple human cell types, we further determine
321 that the sites of m^6A installation are conserved for the most part but that the stoichiometries show cell-
322 type specific differences.

323 Crucially, the inclusion of transcriptome-wide IVT datasets and the use of a selective METTL3 inhibitor
324 (STM2457) provides a robust approach to developing filters that dramatically decrease false-positive m^6A
325 detection. The impact of both approaches was readily visualized by plotting modification probability
326 distributions, enabling our determination that retaining only m^6A calls with confidence scores of 0.98 or
327 greater retained almost all STM2457-sensitive m^6A sites while eliminating the large numbers of false-

positive m^{6}A sites reported for the IVT datasets. This approach is supported by a recent study which highlighted that Dorado introduces large numbers of false positives outside canonical DRACH contexts[35]. Our data confirms that in the unfiltered datasets, the number of false positives is higher in the all-context model compared to the DRACH model. This may reflect the degenerate nature of the canonical DRACH consensus and understudied differences in sequence preference between different cell types and organisms. Retaining only sites at which m^{6}A stoichiometries exceeded 10% further reduced false-positive rates while also focusing the results on identification of sites that are more likely to be biologically significant. The combined effect of these filters was to provide a strong agreement between the m^{6}A all-context and m^{6}A DRACH model in the detection of high confidence m^{6}A sites, as observed by filtering for DRACH motifs from m^{6}A sites detected with the all-context model (**Fig.3B**).

Prior studies have emphasized the need for isoform-resolved m^{6}A quantification by demonstrating widespread heterogeneity in m^{6}A levels between genes and their isoforms[35,36]. Here, we showed that aligning DRS datasets to the human transcriptome reveals differential m^{6}A installation patterns between isoforms, underscoring the importance of accurate, isoform-specific m^{6}A quantification at single-molecule resolution and highlighting the advantage of DRS against short-read sequencing approaches such as GLORI (**Fig. 3E,F**).

Recently, the ability of Dorado and m6Anet[37] to identify m^{6}A in DRS datasets from 293T and HeLa cells were systematically evaluated using IVT RNA and comparisons to published datasets obtained by GLORI and eTAM-seq[23]. In this case the authors found that Dorado (v0.7.2) outperforms m6Anet but also advocated for the importance of applying filters to reduce false positive calls. Likewise, we found that IVT RNA served as a valuable negative control to detect false positive calls. Furthermore, using the RNA calibration strand (RCS) as a negative control provided a convenient and simpler alternative to IVT RNA, yielding comparable probability distributions and thereby enabling a built-in control for routine experiments[21]. While m^{6}A detection was generally reproducible across Dorado versions, model-specific differences are present, i.e. v0.7.0 produces substantially more low-confidence all-context m^{6}A and Ψ calls than v0.8.0–0.9.0, highlighting that the models remain under active development and that benchmarking should be repeated when switching to a new model.

Focusing on other modifications that are detected by Dorado, we observe that inosine and Ψ detection appears robust when applying similar filtering strategies as for m^{6}A, the latter supported by other studies[27,38]. For inosine, we observed an enrichment of high-probability (> 0.99) inosine sites in genome-aligned data from STM2457-treated samples. Further studies are needed to determine whether this

359 reflects increased intron retention or misclassification of modifications by the current inosine model. We
360 also observed a reduction in m^5C sites detected and changes to m^5C stoichiometries in STM2457-treated
361 cells.

362 While DRS is the only approach that allows for robust isoform-specific m^6A mapping, comparisons with
363 orthogonal approaches remain essential to validate findings. When comparing Dorado and GLORI using
364 the same input RNA, we unexpectedly observed that only 50% of m^6A sites with stoichiometries above
365 10% that were identified by Dorado were also present in the GLORI data although increasing the
366 stoichiometries led to increased overlap (**Fig.3D**). We attribute this to a sub-optimal gene-wide adenosine
367 conversion rate of 95% during GLORI, compared to the 98-99% rate reported in the original study[39]. Here,
368 unconverted adenosines result in high signal-to-noise ratios which result in lower sensitivity, explaining
369 why the overlap with Dorado increases at higher-stoichiometry sites. This is also reflected in the relatively
370 high amount of false positive sites detected outside of DRACH motifs in the GLORI datasets (**Fig. 3C**). The
371 sensitivity of GLORI to small fluctuations thus limits its utility in comparison to DRS. Whether this can be
372 resolved with improvements to the GLORI methodology[40] requires further study.

373 Prior analyses of m^6A stoichiometry distributions across immortalized human cell lines, including cancer
374 cell lines, have revealed broadly similar m^6A stoichiometry distributions[36]. By contrast, our analysis of
375 primary fibroblasts (NHDFs) and neuronal cells (differentiated HD10.6 cells) revealed an overall increase
376 in m^6A stoichiometries in neurons compared to fibroblasts, especially in genes associated with neuronal
377 function. While further studies are warranted to establish the underlying mechanisms and functional
378 consequences of these differences, this aligns with the importance of m^6A in neuronal function[41]. This
379 includes m^6A maps from synaptic and nuclear RNA isolated from mouse dorsal hippocampus which
380 showed that synapse-specific RNAs showed generally higher methylation levels[40]. Intriguingly, neuronal
381 regulation pathways utilize differentially spliced isoforms[42] and a recent study revealed isoform-specific
382 differences in m^6A sites and stoichiometries in the human brain that are linked to m^6A machinery
383 expression and cell type context.

384 In summary, using matched RNA samples from different experimental conditions and from different
385 human cell types analyzed with both Dorado and GLORI orthogonal methodologies, we establish a robust
386 pipeline for the precise and quantitative transcriptome-wide detection of m^6A in DRS datasets. Future
387 studies should aim at extending this approach using orthogonal sequencing approaches to benchmark
388 Dorado-based detection of Ψ, m^5C and inosine, as well as the newly released models for 2'O-methylation.

389

390 # Methods

391 **Cell culturing and STM2457 treatment**

392 NHDFs (Lonza) were cultured in Dulbecco's Modified Eagle Medium (DMEM, Gibco), supplemented with
393 5% heat-inactivated FBS (HI-FBS, Gibco) and 1% penicillin-streptomycin (PS, Lonza) under standard culture
394 conditions. The HD10.6 cell line was originally derived from fetal human dorsal root ganglia (DRG) and
395 immortalized by overexpression of the v-myc oncogene under tetracycline regulation. Upon addition of
396 tetracycline and neurotrophins, these cells can be differentiated into neuron-like cells that show typical
397 neuronal morphology and nociceptive properties[28]. For our experiments, we used HD10.6 cells that have
398 been matured for 10 days. For maintenance of undifferentiated HD10.6 cells (a gift from Anna Cliffe,
399 University of Virginia School of Medicine), T-75 flasks were coated with 17 µg/mL fibronectin in PBS for 15
400 min at 37°C before adding the cell suspension. Cells were grown in Advanced DMEM/F12 (Gibco),
401 supplemented with 1x Neurocult SM1 (STEMCELL Technologies), 2 mM L-glutamine (Gibco), 1x Primocin
402 (Invivogen) and 10 ng/mL prostaglandin E1 (Sigma). 0.5 ng/mL bFGF (PeproTech) were added freshly to
403 each media change. For maturation, HD10.6 cells were seeded at a density of 25.000 cells/cm² in 6-well
404 plates which were pre-coated overnight with 50 µg/mL poly-L-ornithine hydrobromide (Sigma) in 0.5M
405 borate buffer pH 8.5 (Boston Bioproducts), and 1 µg/mL fibronectin (overnight). After cell attachment
406 overnight, media was changed to Neurobasal media (Gibco), supplemented with 1x Neurocult SM1, 2mM
407 L-glutamine, 1x Primocin, 1 µg/mL doxycycline, 50 ng/mL NGF (Alomone Labs), and 25 ng/mL CNTF, GDNF
408 and NT-3 (PeproTech). Media was changed every three days until HD10.6 cells showed complete neuronal
409 morphology after 12 days. NHDFs and matured HD10.6 cells were treated with 30 µM STM2457 (Sigma)
410 or DMSO for 48h, harvested in TRIzol (Invitrogen), and stored at -80°C until RNA isolation.

411 **RNA isolation**

412 RNA was extracted by the TRIzol method according to the manufacturer's instructions. Briefly, 0.2 mL
413 chloroform per 1 mL TRIzol were added and mixed by vortexing. After centrifugation for 30 min at 12,000xg
414 at 4°C, the aqueous phase was transferred to isopropanol (0.5 mL per 1 mL TRIzol), mixed and incubated
415 for 10 min at room temperature. Subsequently, the samples were centrifuged for 10 min at 12,000xg at
416 4°C and the RNA pellets were washed twice in 75% fresh ethanol. After air-drying for 5-10 min, RNA was
417 dissolved in nuclease-free H_2O and stored at -80°C until further processing. One third of each sample was
418 used for DRS and the remaining same-input material was processed for GLORI. For both DRS and GLORI,

419 poly(A) RNA was selected using the Dynabeads™ mRNA Purification Kit (Invitrogen), according to the
420 manufacturer's instructions.

421 **GLORI-Sequencing**

422 GLORI reactions were largely performed following the published protocol for RNA protection, deamination
423 and deprotection with several minor adjustments[34]. Briefly, poly(A) RNA was fragmented at 94°C for 2 min
424 (NEB E6150S) and subjected to glyoxal protection, sodium-nitrite-mediated deamination (750 mM $NaNO_2$
425 at 16°C for 8h and 4°C for 6h), and deprotection in triethylammonium acetate-formamide buffer at 95°C
426 for 10 min. Library construction was conducted using a ligation-based strategy as described by Liu and
427 colleagues incorporating 5'adapters with 11-nt UMIs[43].

428 Indexed libraries were amplified with NEBNext Dual Primers Set 2 (E7780S), purified using AMPure XP
429 beads, and validated on an Agilent TapeStation (D1000 High Sensitivity). Sequencing was performed on an
430 Illumina NovaSeq 6000 platform (150 bp paired-end mode; > 80 million reads per sample).

431 For data processing, we employed the same computational pipeline described in Liu et al[43], but
432 implemented within a Snakemake-based framework that automates the complete analysis starting from
433 raw fastq files[44]. Details on software versions, workflow availability, and repository links are provided in
434 the Data and code availability section below.

435

436 **Generation of a transcriptome-wide IVT RNA library**

437 We sequenced the IVT RNA from both NHDFs and HD10.6 cells along with the native poly(A) RNA to
438 evaluate potential false-positive predictions by Dorado. This was achieved by converting the poly(A) RNA
439 to cDNA using a poly(A) primer and a T7-incorporating strand switch primer and using the cDNA as a
440 template for IVT synthesis.

441 **Nanopore Sequencing of poly(A) RNA**

442 Poly(A) RNA was isolated from 22-30 ug total RNA using the Dynabeads™ mRNA Purification Kit
443 (Invitrogen), according to the manufacturer's protocol. 250-300 ng of isolated poly(A) RNA and 25 ng RNA
444 calibration strand (RCS) were used as input for the standard nanopore DRS SQK-RNA004 protocol.
445 Resulting libraries were loaded onto individual PromethION RNA flow cells before sequencing on the
446 PromethION 2 Solo instrument for 48h.

447 **Nanopore basecalling**

448 Basecalling was performed using Dorado v0.5.0, v0.6.0, v0.7.0, v0.8.0 and v0.9.0 (ONT) in super accuracy
449 mode with modification detection enabled for m^6A (DRACH context) in v.0.5.0, 0.6.0, 0.8.0 and 0.9.0, m^6A
450 (all context) in v0.7.0, 0.8.0 and 0.9.0, Ψ in v0.7.0, v0.8.0 and v0.9.0. Each dataset was processed with
451 adapter trimming. Resulting unaligned BAM files were converted to FASTQ files containing modification
452 tags for every read in the FASTQ read headers, using SAMtools v1.18[45] [*samtools fastq -TMM,ML*].
453

454 **Genome and transcriptome level alignments**

455 For genome-level alignment, reads were aligned against a combined human genome reference
456 (GRCh38.p14), and the RCS gene sequence, using minimap2 v2.26 [*minimap2 -ax splice -k14 -y -uf --*
457 *secondary=no*]. For transcriptome-level alignment, the reads were aligned against the human
458 transcriptome (v47), obtained via GENCODE[46] [*minimap2 -t 8 -ax map-ont -y -L -p 0.99*]. Using SAMtools
459 v1.18, resulting genome- and transcriptome-aligned SAM files were converted to BAM files retaining only
460 primary alignments [*samtools view -b -F2308* and *samtools view -b -F2324,* respectively]. BAM files were
461 sorted [*samtools sort*] and indexed [*samtools index*].

462 **Processing of RNA modification calls using Modkit**

463 Probability distributions of the detected sites in human genome- and transcriptome-aligned reads were
464 generated using sample-probs subcommand from Modkit v0.4.1[31] [sample-probs --hist --only-mapped --
465 percentiles 0.1,0.2,0.3,0.4,0.5,0.6,0.7,0.8,0.85,0.9 -f 0.1]. For RCS reads -f value was increased to 0.25. The
466 resulting .tsv files were imported into RStudio (v. 2024.12.1+563) and plotted using a custom R(v. 4.4.2)
467 script (Dorado_mod_probability_distributions.R), with the following packages: dplyr (v1.1.4), ggplot2
468 (v3.5.1), reshape2 (v1.4.4), patchwork (v1.3.0).

469 To generate extended bedMethyl files with m^6A-modified and unmodified base counts from the reads
470 mapping against the potential modification sites, we used Modkit pileup subcommand with the thresholds
471 [*--filter-threshold A:0.8 --filter-threshold T:0.8 --filter-threshold C:0.8 --filter-threshold G:0.8 --motif A 0 --*
472 *ref $REF*] with and without modification threshold filter [*--mod-thresholds a:0.98*] to generate our
473 "filtered" and "unfiltered" datasets, respectively. Canonical nucleotide calls (A, C, G, U) were retained with
474 > 80% probability scores for all modification datasets. Modification thresholds were set at 98% for m^6A
475 and 99% for all the other modifications. *--motif* was adjusted to the base for which modification status
476 was examined, which further restricted the analysis to only the positions that matched canonical

477 nucleotides in the reference genome. The resulting sites were further filtered according to the read
478 number per site (≥ 20 reads) for all the downstream analysis.

479 **Gene Ontology analysis**

480 GO analysis was performed using DAVID[47]. Genes harboring m^6A sites were filtered for genes that were
481 generally present in both datasets. Next, they were divided into NHDF-specific, HD10.6-specific, and
482 shared categories, and enrichment was assessed for biological processes. GO terms were considered
483 significant at FDR ≤ 0.05 with a minimum of 20 genes per GO term. For plotting, the top 20 GO terms that
484 contained the highest gene numbers were extracted from the analysis of the shared gene sets.

485 **Analysis and visualization of modification stoichiometries and distributions**

486 Stoichiometry distribution histograms and metaplots were generated using Rstudio and R v4.4.2 with the
487 following libraries: data.table, patchwork, scales, tidyr, dplyr, ggplot2[4]. Access to scripts used for analysis
488 and visualization is detailed below.
489

490 **Data and code availability**

491 Raw fastq and pod5 datasets generated in this study are available via the European Nucleotide Archive
492 (ENA) under the accession number PRJEB101380.
493 R scripts used in the analysis and visualization of data presented herein are available in the
494 https://github.com/DepledgeLab/HOLDEN repository.
495 The Snakemake workflow implementing the GLORI analysis pipeline is available in the
496 https://github.com/gp-micro/glori repository.

497

498 **Acknowledgements and funding**

499 DPD is supported by a German Centre for Infection Research (DZIF) Associate Professorship and the NIAID
500 grants R01-AI170583 and R01-AI152543. DPD also receives funding from the Deutsche
501 Forschungsgemeinschaft (DFG, German Research Foundation) under Germany's Excellence Strategy - EXC
502 2155, project number 390874280. EL is supported by the NIAID grant R01-AI170583 as well as the
503 Hannover Biomedical Research School (HBRS) and the Center for Infection Biology (ZIB). DO is supported
504 by the Walter Benjamin Programme of the DFG, project 554758329. ACW is supported by NIAID grants
505 R01AI176335 and R01-AI170583.

References

1 Gilbert, W. V. & Nachtergaele, S. mRNA Regulation by RNA Modifications. *Annu Rev Biochem* **92**, 175-198 (2023). https://doi.org:10.1146/annurev-biochem-052521-035949

2 Cappannini, A. *et al.* MODOMICS: a database of RNA modifications and related information. 2023 update. *Nucleic Acids Research* **52**, D239-D244 (2023). https://doi.org:10.1093/nar/gkad1083

3 Anreiter, I., Mir, Q., Simpson, J. T., Janga, S. C. & Soller, M. New Twists in Detecting mRNA Modification Dynamics. *Trends Biotechnol* **39**, 72-89 (2021). https://doi.org:10.1016/j.tibtech.2020.06.002

4 Yang, L. *et al.* Emerging role of RNA modification and long noncoding RNA interaction in cancer. *Cancer Gene Ther* **31**, 816-830 (2024). https://doi.org:10.1038/s41417-024-00734-2

5 Zaccara, S., Ries, R. J. & Jaffrey, S. R. Reading, writing and erasing mRNA methylation. *Nature Reviews Molecular Cell Biology* **20**, 608-624 (2019). https://doi.org:10.1038/s41580-019-0168-5

6 Murakami, S. & Jaffrey, S. R. Hidden codes in mRNA: Control of gene expression by m(6)A. *Mol Cell* **82**, 2236-2251 (2022). https://doi.org:10.1016/j.molcel.2022.05.029

7 He, P. C. & He, C. m(6) A RNA methylation: from mechanisms to therapeutic potential. *Embo j* **40**, e105977 (2021). https://doi.org:10.15252/embj.2020105977

8 Gilbert, W. V. & Nachtergaele, S. mRNA Regulation by RNA Modifications. *Annual Review of Biochemistry* **92**, 175-198 (2023). https://doi.org:https://doi.org/10.1146/annurev-biochem-052521-035949

9 Sendinc, E. & Shi, Y. RNA m6A methylation across the transcriptome. *Mol Cell* **83**, 428-441 (2023). https://doi.org:10.1016/j.molcel.2023.01.006

10 Sun, H., Li, K., Liu, C. & Yi, C. Regulation and functions of non-m(6)A mRNA modifications. *Nat Rev Mol Cell Biol* **24**, 714-731 (2023). https://doi.org:10.1038/s41580-023-00622-x

11 Moshitch-Moshkovitz, S. *et al.* mRNA m6A detection. *Nature Reviews Methods Primers* **4** (2024). https://doi.org:10.1038/s43586-024-00365-9

12 Dominissini, D. *et al.* Topology of the human and mouse m6A RNA methylomes revealed by m6A-seq. *Nature* **485**, 201-206 (2012). https://doi.org:10.1038/nature11112

13 Meyer, Kate D. *et al.* Comprehensive Analysis of mRNA Methylation Reveals Enrichment in 3' UTRs and near Stop Codons. *Cell* **149**, 1635-1646 (2012). https://doi.org:https://doi.org/10.1016/j.cell.2012.05.003

14 Linder, B. *et al.* Single-nucleotide-resolution mapping of m6A and m6Am throughout the transcriptome. *Nature Methods* **12**, 767-772 (2015). https://doi.org:10.1038/nmeth.3453

15 Meyer, K. D. DART-seq: an antibody-free method for global m6A detection. *Nature Methods* **16**, 1275-1280 (2019). https://doi.org:10.1038/s41592-019-0570-0

16 Xiao, Y. L. *et al.* Transcriptome-wide profiling and quantification of N(6)-methyladenosine by enzyme-assisted adenosine deamination. *Nat Biotechnol* **41**, 993-1003 (2023). https://doi.org:10.1038/s41587-022-01587-6

17 Liu, C. *et al.* Absolute quantification of single-base m(6)A methylation in the mammalian transcriptome using GLORI. *Nat Biotechnol* **41**, 355-366 (2023). https://doi.org:10.1038/s41587-022-01487-9

18 Diensthuber, G. & Novoa, E. M. Charting the epitranscriptomic landscape across RNA biotypes using native RNA nanopore sequencing. *Mol Cell* **85**, 276-289 (2025). https://doi.org:10.1016/j.molcel.2024.12.014

19 Garalde, D. R. *et al.* Highly parallel direct RNA sequencing on an array of nanopores. *Nat Methods* **15**, 201-206 (2018). https://doi.org:10.1038/nmeth.4577

20 Jain, M., Olsen, H. E., Paten, B. & Akeson, M. The Oxford Nanopore MinION: delivery of nanopore sequencing to the genomics community. *Genome Biology* **17**, 239 (2016). https://doi.org:10.1186/s13059-016-1103-0

21 Viehweger, A. *et al.* Direct RNA nanopore sequencing of full-length coronavirus genomes provides novel insights into structural variants and enables modification analysis. *Genome Res* **29**, 1545-1554 (2019). https://doi.org:10.1101/gr.247064.118

22 Abebe, J. S., Verstraten, R. & Depledge, D. P. Nanopore-Based Detection of Viral RNA Modifications. *mBio* **13**, e03702-03721 (2022). https://doi.org:doi:10.1128/mbio.03702-21

23 Zou, Y. *et al.* A comparative evaluation of computational models for RNA modification detection using nanopore sequencing with RNA004 chemistry. *Briefings in Bioinformatics* **26** (2025). https://doi.org:10.1093/bib/bbaf404

24 Cruciani, S. & Novoa, E. M. The new era of single-molecule RNA modification detection through nanopore base-calling models. *Nat Rev Mol Cell Biol* (2025). https://doi.org:10.1038/s41580-025-00896-3

25 Cruciani, S. *et al.* De novo basecalling of RNA modifications at single molecule and nucleotide resolution. *Genome Biol* **26**, 38 (2025). https://doi.org:10.1186/s13059-025-03498-6

26 Diensthuber, G. & Novoa, E. M. Charting the epitranscriptomic landscape across RNA biotypes using native RNA nanopore sequencing. *Molecular Cell* **85**, 276-289 (2025). https://doi.org:https://doi.org/10.1016/j.molcel.2024.12.014

27 Esfahani, N. G., Stein, A. J., Akeson, S., Tzadikario, T. & Jain, M. Evaluation of Nanopore direct RNA sequencing updates for modification detection. *bioRxiv* (2025). https://doi.org:10.1101/2025.05.01.651717

28 Raymon, H. K. *et al.* Immortalized Human Dorsal Root Ganglion Cells Differentiate into Neurons with Nociceptive Properties. *The Journal of Neuroscience* **19**, 5420-5428 (1999). https://doi.org:10.1523/jneurosci.19-13-05420.1999

29 Yankova, E. *et al.* Small-molecule inhibition of METTL3 as a strategy against myeloid leukaemia. *Nature* **593**, 597-601 (2021). https://doi.org:10.1038/s41586-021-03536-w

30 Yang, Y. *et al.* Current progress in strategies to profile transcriptomic m(6)A modifications. *Front Cell Dev Biol* **12**, 1392159 (2024). https://doi.org:10.3389/fcell.2024.1392159

31 *https://github.com/nanoporetech/modkit*.

32 Xu, H. *et al.* Absolute quantitative and base-resolution sequencing reveals comprehensive landscape of pseudouridine across the human transcriptome. *Nat Methods* **21**, 2024-2033 (2024). https://doi.org:10.1038/s41592-024-02439-8

33 Xie, Y.-Y. *et al.* Single-molecule direct RNA sequencing reveals the shaping of epitranscriptome across multiple species. *Nature Communications* **16**, 5119 (2025). https://doi.org:10.1038/s41467-025-60447-4

34 Shen, W. *et al.* GLORI for absolute quantification of transcriptome-wide m(6)A at single-base resolution. *Nat Protoc* **19**, 1252-1287 (2024). https://doi.org:10.1038/s41596-023-00937-1

35 Xie, Y. Y. *et al.* Single-molecule direct RNA sequencing reveals the shaping of epitranscriptome across multiple species. *Nat Commun* **16**, 5119 (2025). https://doi.org:10.1038/s41467-025-60447-4

36 Guo, W. *et al.* Single-molecule m6A detection empowered by endogenous labeling unveils complexities across RNA isoforms. *Molecular Cell* (2025). https://doi.org:https://doi.org/10.1016/j.molcel.2025.01.014

37 Hendra, C. *et al.* Detection of m6A from direct RNA sequencing using a multiple instance learning framework. *Nature Methods* **19**, 1590-1598 (2022). https://doi.org:10.1038/s41592-022-01666-1

38 Verstraten, R. *et al.* Defining expansions and perturbations to the RNA polymerase III transcriptome and epitranscriptome by modified direct RNA nanopore sequencing. *bioRxiv* (2025). https://doi.org:10.1101/2025.03.07.641986

39 Shen, W. *et al.* GLORI for absolute quantification of transcriptome-wide m6A at single-base resolution. *Nature Protocols* **19**, 1252-1287 (2024). https://doi.org:10.1038/s41596-023-00937-1

40 Sun, H. *et al.* Mild and ultrafast GLORI enables absolute quantification of m6A methylome from low-input samples. *Nature Methods* **22**, 1226-1236 (2025). https://doi.org:10.1038/s41592-025-02680-9

41 Yu, J., She, Y. & Ji, S.-J. m6A Modification in Mammalian Nervous System Development, Functions, Disorders, and Injuries. *Frontiers in Cell and Developmental Biology* **Volume 9 - 2021** (2021). https://doi.org:10.3389/fcell.2021.679662

42 Su, C.-H., D, D. & Tarn, W.-Y. Alternative Splicing in Neurogenesis and Brain Development. *Frontiers in Molecular Biosciences* **Volume 5 - 2018** (2018). https://doi.org:10.3389/fmolb.2018.00012

43 Liu, J. F., Hawley, B. R., Nicholson, L. S. & Jaffrey, S. R. Decoding m(6)Am by simultaneous transcription-start mapping and methylation quantification. *Elife* **13** (2025). https://doi.org:10.7554/eLife.104139

44 Köster, J. & Rahmann, S. Snakemake--a scalable bioinformatics workflow engine. *Bioinformatics* **28**, 2520-2522 (2012). https://doi.org:10.1093/bioinformatics/bts480

45 Li, H. *et al.* The Sequence Alignment/Map format and SAMtools. *Bioinformatics* **25**, 2078-2079 (2009). https://doi.org:10.1093/bioinformatics/btp352

46 Mudge, J. M. *et al.* GENCODE 2025: reference gene annotation for human and mouse. *Nucleic Acids Res* **53**, D966-d975 (2025). https://doi.org:10.1093/nar/gkae1078

47 Huang da, W., Sherman, B. T. & Lempicki, R. A. Systematic and integrative analysis of large gene lists using DAVID bioinformatics resources. *Nat Protoc* **4**, 44-57 (2009). https://doi.org:10.1038/nprot.2008.211

Figure legends

Figure 1. Workflow for m^{6}A mapping in different human cell types using orthogonal sequencing approaches.

(A) Schematic of the experimental setup. RNA was isolated from NHDFs and differentiated HD10.6 cells treated with STM2457 or DMSO for 48h. Poly(A) RNA was subjected to DRS and GLORI from the same input material. IVT RNA was generated in parallel to assess potential false-positive modification calls. **(B)** Workflow for benchmarking Dorado basecalling. Reads were processed with Dorado versions v.0.5.0 through v0.9.0, aligned to the human genome or transcriptome, and analyzed with ONT's Modkit tool. Multiple filtering strategies were tested against IVT controls and METTL3 inhibition (STM2457). Resulting

641 m^{6}A sites were compared with GLORI data from the same input RNA. **(C)** Final benchmarked Dorado
642 pipeline to detect high-confidence m^{6}A sites.

643

644 **Figure 2. Modification probability of 0.98 and stoichiometry score of ≥10% are necessary cutoffs to**
645 **identify m^{6}A sites accurately.**

646 **(A)** Dorado v0.9.0-generated modification probability distributions for all-context m^{6}A from genome-
647 aligned DMSO- and STM2457-treated NHDFs plotted against the ones from in vitro transcribed (IVT) NHDF
648 poly(A) RNA. DMSO probability score distribution is shown as a red solid line, STM2457 – red dashed line,
649 IVT – grey solid line. **(B)** Same as in (A), but for DRACH-context m^{6}A sites. **(C)** Stoichiometry (≥10%)
650 distributions for all-context m^{6}A from DMSO- (in red) or STM2457-treated (in pink) NHDF datasets
651 (genome-aligned) are plotted using a 0.98 modification probability cutoff and a filter for ≥ 20 reads. **(D)**
652 Same as in (C), but for DRACH-context m^{6}A sites. **(E)** Overlap of m^{6}A sites between all-context and DRACH
653 models (A basecall accuracy ≥80%, coverage ≥20reads, stoichiometry ≥10%), comparing non-filtered to
654 filtered (modification probability >0.98) outputs. **(F)** Metagene plots showing the density of m^{6}A (all-
655 context – dark red, DRACH-context – bright red) sites across all annotated poly(A) transcripts (left) and
656 monoexonic poly(A) transcripts (right) from genome-aligned DMSO-treated NHDF datasets filtered with
657 0.98 modification probability, ≥20 coverage and ≥10% stoichiometry.

658

659 **Figure 3. Comparison of m^{6}A sites detected by Dorado and GLORI.**

660 **(A)** Filtering strategy for ONT's Dorado and GLORI to obtain a high-confidence list of m^{6}A sites in NHDFs.
661 **(B)** Stoichiometry distributions are plotted from genome-aligned DMSO- or STM2457-treated NHDF
662 datasets using the indicated Dorado models and the filtering strategy shown in (A). **(C)** Stoichiometry
663 distributions from GLORI performed on DMSO- or STM2457-treated NHDFs are plotted, using the filtering
664 strategy shown in (A). In addition, m^{6}A sites were filtered for DRACH motifs (right plot). **(D)** Overlap of
665 high-confidence m^{6}A sites detected by Dorado vs GLORI. GLORI datasets were filtered using increasing m^{6}A
666 stoichiometry cutoffs (from left to right). **(E)** m^{6}A sites in the *SPEN* gene detected by GLORI and Dorado.
667 Boxplots (right) represent the m^{6}A stoichiometries per m^{6}A site shown on the left. **(F)** *SPEN* isoforms with
668 m^{6}A sites, determined by Dorado. Boxplots (right) show the distribution of m^{6}A stoichiometries on the
669 m^{6}A sites on *SPEN-201* and *SPEN-202*.

670

671 **Figure 4. Comparative analysis of m^{6}A modification patterns in NHDFs and HD10.6 cells using Dorado**
672 **v0.9.0.**
673 **(A)** Overlap of high-confidence m^{6}A sites between NHDFs and HD10.6 cells. **(B)** Correlation of shared m^{6}A
674 stoichiometries (n=38,217). **(C)** GO term analysis (Biological Process, DAVID Bioinformatics Resources) of
675 genes with shared or unique m^{6}A sites. **(D+E)** Motif analysis showing m^{6}A (all-context and DRACH-context)
676 motif logos, 5-mer distributions and modification stoichiometries in NHDFs. **(F+G)** Same as in (D+E) but for
677 HD10.6 cells. **(H)** KEGG pathway analysis (DAVID Bioinformatics Resources) of shared m^{6}A-containing
678 genes. **(I)** m^{6}A stoichiometries of representative examples of individual genes from enriched pathways (H).
679 *ACTG1* serves as a housekeeping control.
680

Figure S1. Evaluation of Dorado by base and modification probability distributions.

(A) Dorado v0.9.0-generated basecall accuracy probability values for A (all-context and DRACH-context basecaller models) from genome-aligned DMSO- and STM2457-treated NHDF samples against in vitro transcribed poly(A) NHDF RNA. A probability score distribution is shown as a black solid line for DMSO, STM2457 – black dashed line, IVT – grey solid line. **(B)** Dorado v0.9.0-generated modification probability distributions, visualized as histograms, for all-context m6A from genome-aligned DMSO- and STM2457-treated NHDFs and in vitro transcribed (IVT) NHDFs. IVT modification probability score distribution is shown in grey, DMSO – bright red, STM2457 – dark red. **(C)** Same as in (B), but for DRACH-context m6A sites.

Figure S2. Modification probability cutoffs are necessary to identify Ψ and inosine sites more accurately.

(A) Dorado v0.9.0-generated basecall accuracy probability values for U (left) and modification probability distributions for Ψ (right) from genome-aligned DMSO- and STM2457-treated NHDF samples are plotted against in vitro transcribed poly(A) RNA. Ψ probabilities are visualized in blue solid and dashed lines for DMSO and STM2457, respectively and in grey solid line for IVT. **(B)** Same as in (A), but showing A base accuracy probabilities and inosine sites. Inosine probabilities are visualized in purple solid and dashed lines for DMSO and STM2457, respectively and in grey solid line for IVT. **(C)** Same as in (A), but showing C base accuracy probabilities and m^5C sites. m^5C probabilities are visualized in green solid and dashed lines for DMSO and STM2457, respectively and in grey solid line for IVT. **(D+E)** DRACH-context and all-context m^6A modification probability distributions (red) from genome-aligned DMSO- and STM2457-treated NHDFs are plotted against RCS negative control (grey).

Figure S3. Modification probability cutoffs are necessary to identify modification sites accurately, shown for transcriptome-aligned data.

Dorado v0.9.0-generated basecall accuracy probability values for A, U and C (left, **A-E**) and modification probability distributions for m^6A (all-context), m^6A (DRACH-context), Ψ, inosine and m^5C (right, **A-E**) in transcriptome-aligned DMSO-and STM2457-treated NHDFs, plotted against the values from in vitro transcribed (IVT) NHDF poly(A) RNA.

Figure S4. Modification probability distribution profiles in genome-aligned DMSO-and STM2457-treated HD10.6 cells.

Dorado v0.9.0-generated basecall accuracy probability values for A, U and C (left, **A-E**) and modification probability distributions for m^6A (all-context), m^6A (DRACH-context), Ψ, inosine and m^5C (right, **A-E**) in human genome-aligned DMSO-and STM2457-treated HD10.6 cells, plotted against the values from in vitro transcribed (IVT) NHDF poly(A) RNA.

Figure S5. Modification probability distribution profiles in transcriptome-aligned DMSO-and STM2457-treated HD10.6 cells.

Dorado v0.9.0-generated basecall accuracy probability values for A, U and C (left, **A-E**) and modification probability distributions for m^6A (all-context), m^6A (DRACH-context), Ψ, inosine and m^5C (right, **A-E**) in human transcriptome-aligned DMSO-and STM2457-treated HD10.6 cells, plotted against the values from in vitro transcribed (IVT) NHDF poly(A) RNA.

Figure S6. Modification site probabilities detected with different versions of Dorado and compared to RCS.

(A+B) DRACH-context and all-context m^6A modification probability distributions (red) from genome-aligned DMSO- and STM2457-treated NHDFs are plotted against RCS negative control (grey). **(C)** Modification probability distributions for all-context m^6A (Dorado v0.7.0, v0.8.0 and v0.9.0), the bottom panel showing the distributions in 0.95-1.00 modification range. **(D)** Same as in (C), but for DRACH-context m^6A (Dorado v0.5.0, v0.6.0, v0.8.0 and v0.9.0). **(E)** Same as in (C), but for Ψ (Dorado v0.7.0, v0.8.0, v0.9.0). All the plots in C-E are generated from genome-aligned DMSO-treated NHDF datasets and are plotted against RCS negative controls.

Figure S7. Evaluation of Dorado by stoichiometry distributions.

(A) Stoichiometry distributions for all-context m^6A from DMSO- (in red) or STM2457-treated (in pink) NHDF datasets (genome-aligned and filtered for ≥ 20 reads) are plotted, comparing 0.98 modification probability-unfiltered (left) and filtered (right) sites. **(B)** Same as in (A), but for DRACH-context m^6A sites.

Figure S8. Stoichiometry distributions of m^6A, Ψ and inosine in IVT datasets.

(A) All-context m^6A stoichiometry distributions (all stoichiometries (top) and ≥10% stoichiometries (bottom)) in (genome-aligned) IVT from DMSO-treated NHDFs, comparing 0.98 modification probability-unfiltered and filtered data. The bottom panel shows stoichiometry distributions only for ≥10% stoichiometry sites. **(B)** As in (A), but for DRACH-context m6A. **(C)** As in (A), but for Ψ. **(D)** As in (A), but for inosine.

Figure S9. Evaluation of Dorado by stoichiometry distributions in transcriptome-aligned NHDFs.

(A) Stoichiometry distributions for all-context m^6A from DMSO- (in red) or STM2457-treated (in pink) NHDF datasets (transcriptome-aligned and filtered for ≥ 20 reads) are plotted, assessing the 0.98 modification probability cutoff. The bottom panel shows stoichiometry distributions only for ≥10% stoichiometry sites. **(B)** Same as in (A), but for DRACH-context m^6A sites.

Figure S10. Evaluation of Dorado by stoichiometry distributions in transcriptome-aligned HD10.6 cells.

(A) Stoichiometry distributions for all-context m^6A from DMSO- (in red) or STM2457-treated (in pink) HD10.6 datasets (transcriptome-aligned and filtered for ≥ 20 reads) are plotted, assessing the 0.98

modification probability cutoff. The bottom panel shows stoichiometry distributions only for ≥10% stoichiometry sites. **(B)** Same as in (A), but for DRACH-context m^6A sites.

Figure S11 Stoichiometry distributions of Ψ and inosine in NHDFs.

(A) Distributions of all (left) and ≥10% (right) Ψ stoichiometries in the 0.99 modification probability-unfiltered and filtered data from genome-aligned DMSO- (darker color) and STM2457-treated (lighter color) NHDFs (filtered for ≥20 reads). **(B)** Same as in (A), but for inosine.

Figure S12. Stoichiometry distributions of Ψ and inosine in HD10.6 cells.

(A) Distributions of all and ≥10% Ψ stoichiometries in the 0.99 modification probability-unfiltered and filtered data from genome-aligned DMSO- (darker color) and STM2457-treated (lighter color) HD10.6 cells (filtered for ≥20 reads). **(B)** Same as in (A), but for inosine.

Figure S13. m^6A and Ψ stoichiometry distributions in different versions of Dorado.

Stoichiometry distributions (all stoichiometries – left, ≥10% stoichiometries – right) in a line graph format for **(A)** all-context m^6A detected in genome-aligned DMSO-treated NHDF dataset, with Dorado versions 0.7.0, 0.8.0 and 0.9.0 colored in gradients of red, darkness increasing with the later versions. **(B)** DRACH-context m^6A detected with Dorado versions 0.5.0, 0.6.0, 0.8.0 and 0.9.0, colored in gradients of red, darkness increasing with the later versions. **(C)** Ψ detected with Dorado versions 0.7.0, 0.8.0 and 0.9.0, colored in gradients of blue, darkness increasing with the later versions. All the datasets were filtered for ≥20 reads.

Figure S14. Comparison of modification sites detected with different versions of Dorado.

Upset plots showing unique and shared detected modifications (filtered for ≥20 reads, ≥10% stoichiometry) in modification probability-unfiltered and filtered genome-aligned DMSO-treated NHDF data. The versions are ordered on the plot by the number of detected sites, in ascending order (on the left). Results are shown for the following models and versions: **(A)** all-context m^6A detected with v.0.7.0, v0.8.0 and v0.9.0, **(B)** DRACH-context m^6A detected with v.0.5.0, v0.6.0, v0.8.0 and v0.9.0, **(C)** Ψ detected with v.0.7.0, v0.8.0 and v0.9.0. **(D)** Nucleotide frequencies in the 5-base motif of Ψ sites for uniquely v0.7.0-, v0.8.0-0.9.0- and v0.7.0-0.8.0-0.9.0-detected Ψ sites. Position 0 marks the modification site.

Figure S15. m^6A (all-context and DRACH-context) motif logos for modification probability-unfiltered NHDF and HD10.6 data.

(A) 5-mer motif logo (showing nucleotide frequences at each position) of m^6A-modified sites (position 0 = modified A) from genome-aligned DMSO-treated NHDFs (all-context – left, DRACH-context – right). All the datasets were filtered for ≥20 coverage & ≥10% stoichiometry. **(B)** Same as (A), but for HD10.6 cells.

Figure S16. Metagene plots showing m^6A (all-context and DRACH-context) distribution profiles in NHDF and HD10.6 data filtered at different stoichiometries.

(A) The density of all-context m^6A sites (0.98 modification probability-unfiltered – left, filtered – right) plotted across all annotated poly(A) transcripts of NHDF (dark red) and HD10.6 (bright red) datasets, filtered with different stoichiometries (descending: all stoichiometries, ≥50%, ≥10%, <10% and ≤5%). All datasets were filtered additionally for ≥20 coverage & ≥10% stoichiometry. **(B)** Same as (A), but for DRACH-context m^6A sites.

Figure S17. Comparison of m^6A sites detected by Dorado and GLORI-Sequencing in NHDFs and HD10.6s.

(A) Upset plot showing the number of m^6A sites detected by GLORI and Dorado in NHDFs and their overlaps. Dorado sites represent high-confidence m^6A sites obtained after filtering DRACH-model detected data. Similarly, only high-confidence m^6A sites detected by GLORI are shown, but were additionally filtered for DRACH sites. **(B)** Stoichiometry distributions are plotted from genome-aligned DMSO- or STM2457-treated HD10.6 datasets using the indicated Dorado models. **(C)** Stoichiometry distributions from GLORI performed on DMSO- or STM2457-treated NHDFs are plotted. In addition, m^6A sites were filtered for DRACH motifs (right plot). **(D)** Stoichiometry distributions are plotted from transcriptome-aligned DMSO- or STM2457-treated NHDF datasets using the indicated Dorado models. **(E)** Stoichiometry distributions are plotted from transcriptome-aligned DMSO- or STM2457-treated HD10.6 datasets using the indicated Dorado models.

Figure 1

A

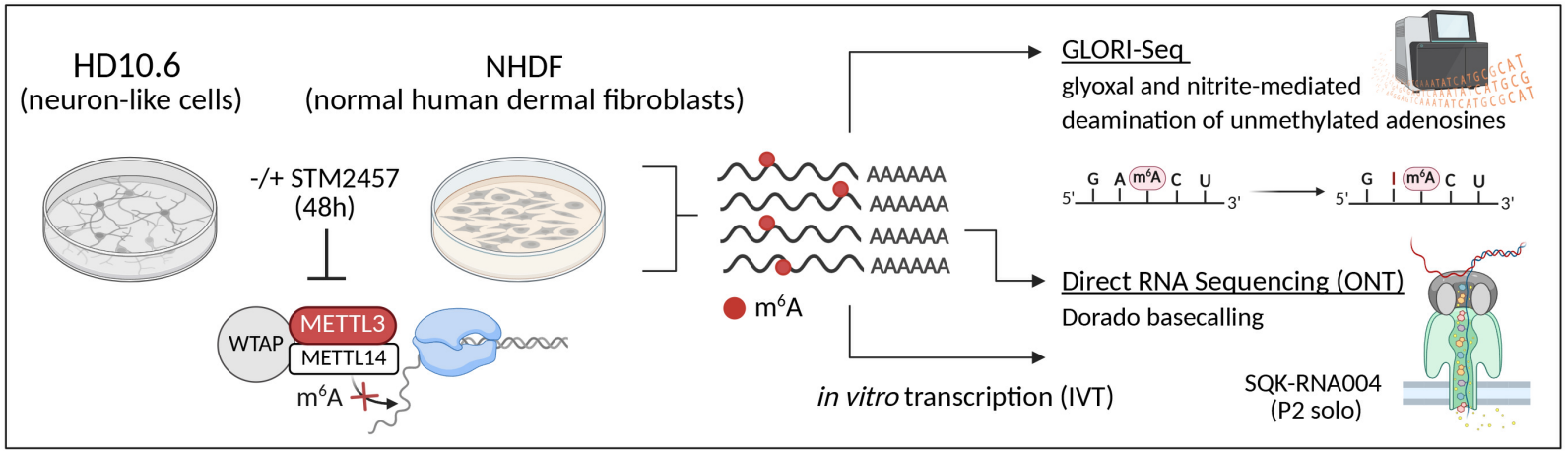

B

ONT DRS (P2 solo) and Dorado

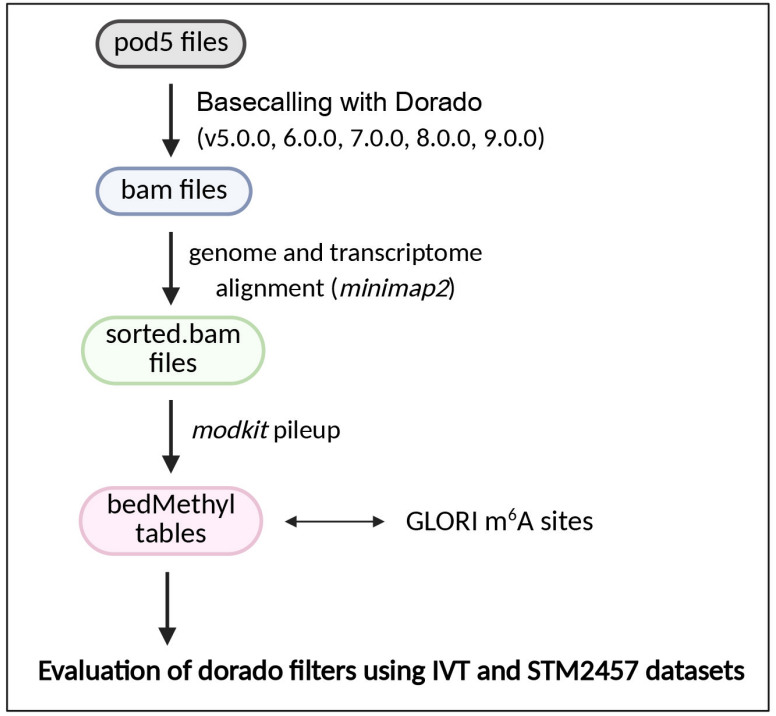

C

Benchmarked m^{6}A Dorado pipeline

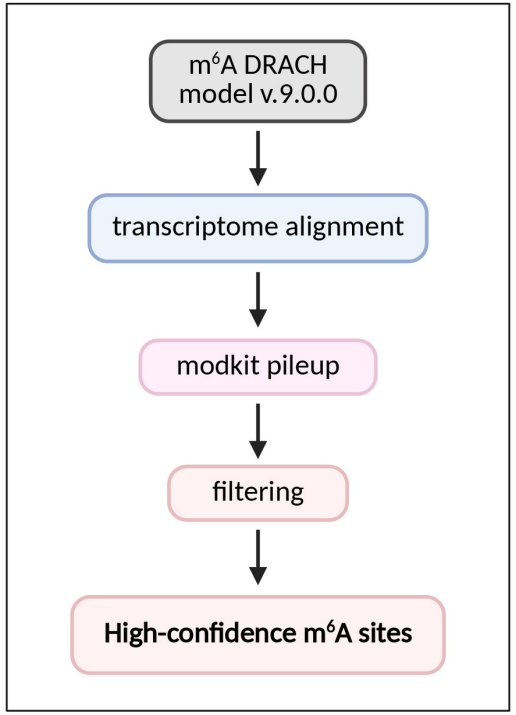

Figure 2

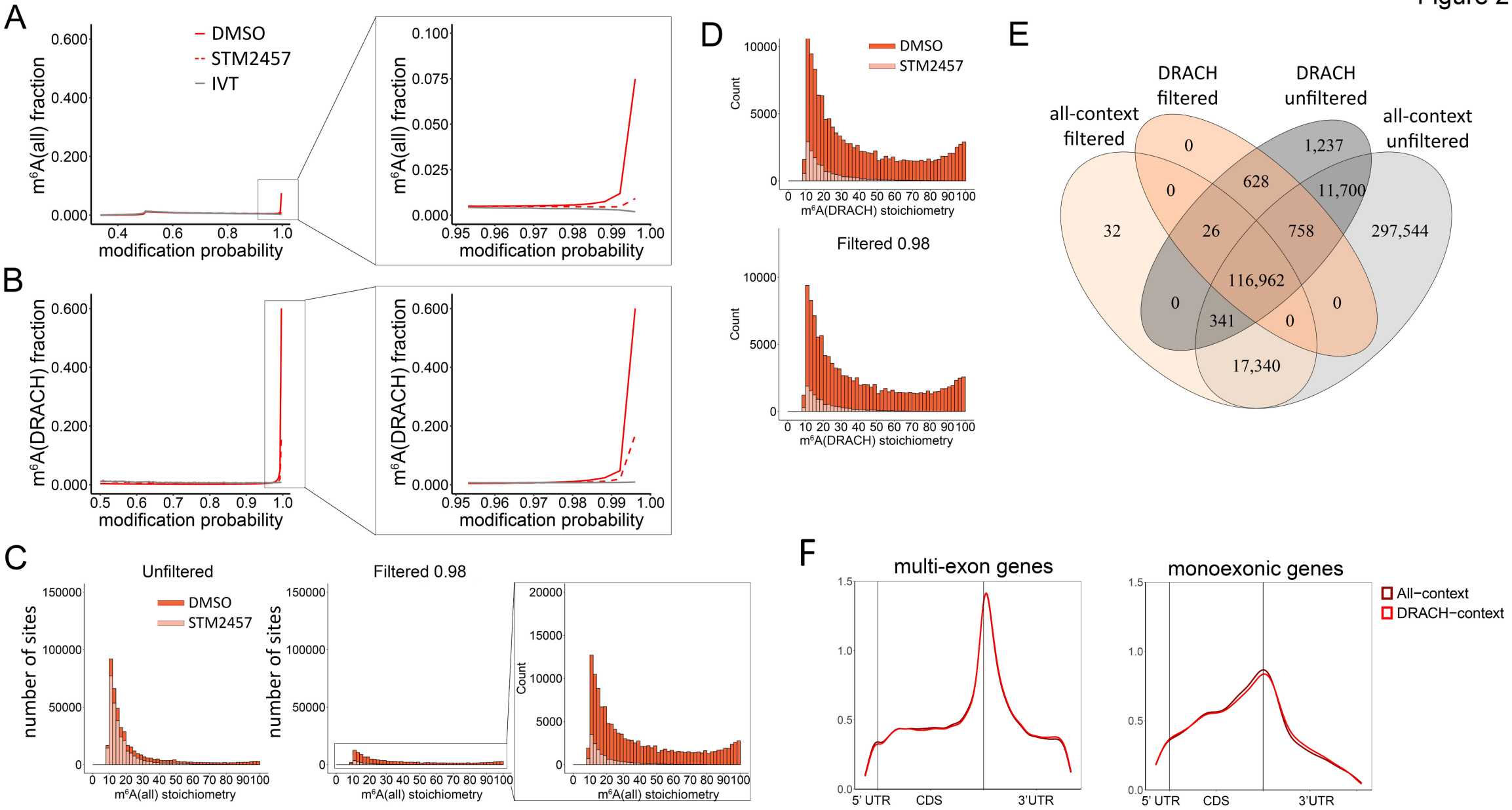
A
DMSO
STM2457
IVT
m6A(all) fraction
modification probability
B
m6A(DRACH) fraction
modification probability
C
Unfiltered
Filtered 0.98
DMSO
STM2457
number of sites
Count
m6A(all) stoichiometry
D
DMSO
STM2457
Count
m6A(DRACH) stoichiometry
Filtered 0.98
E
all-context filtered
DRACH filtered
DRACH unfiltered
all-context unfiltered
32
0
0
628
1,237
11,700
26
758
297,544
116,962
0
341
0
0
17,340
F
multi-exon genes
monoexonic genes
All−context
DRACH−context
5' UTR
CDS
3'UTR

Figure 3

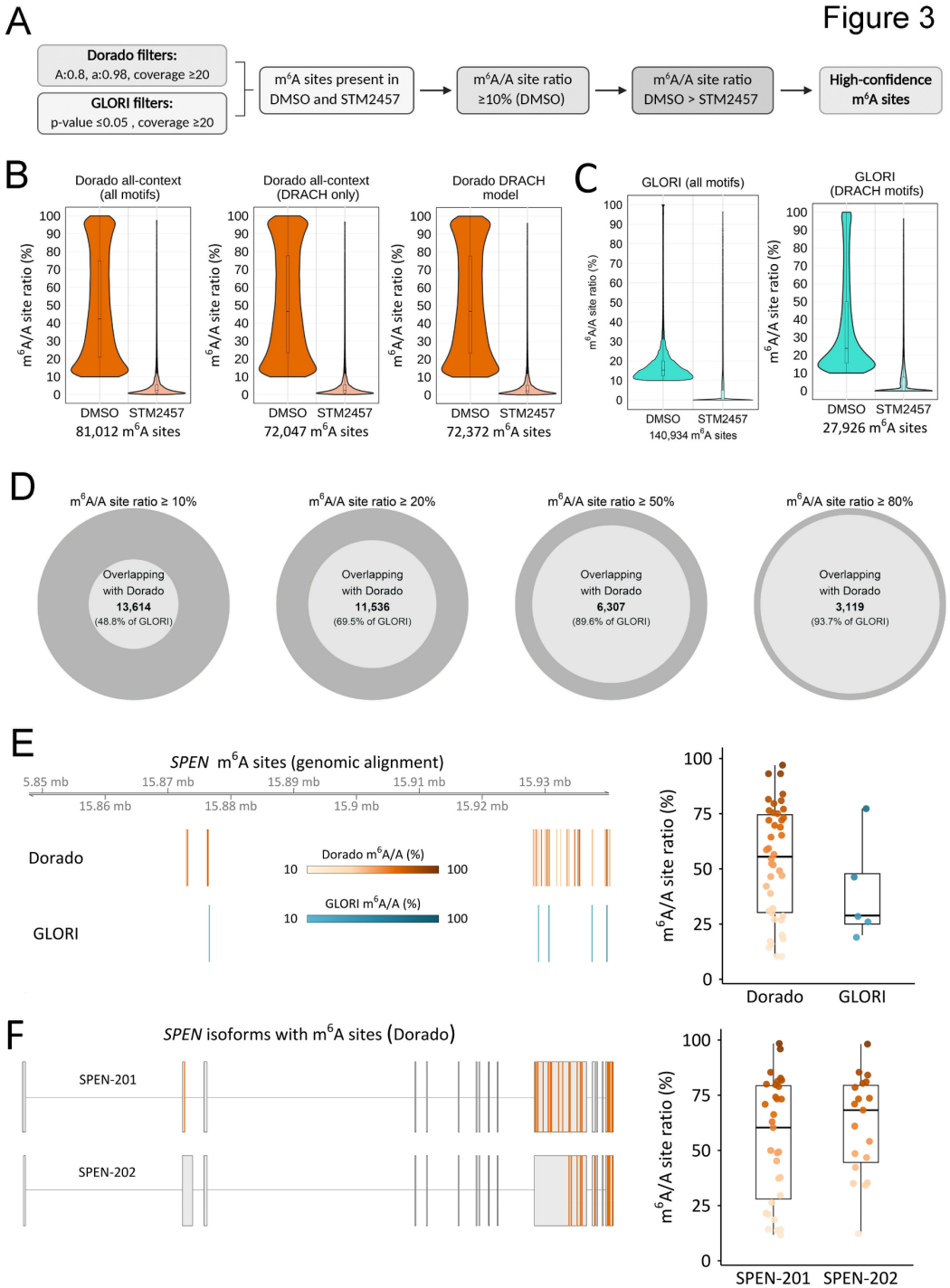
A
Dorado filters:
A:0.8, a:0.98, coverage ≥20
GLORI filters:
p-value ≤0.05 , coverage ≥20
m6A sites present in DMSO and STM2457
m6A/A site ratio ≥10% (DMSO)
m6A/A site ratio DMSO > STM2457
High-confidence m6A sites
B
Dorado all-context (all motifs)
Dorado all-context (DRACH only)
Dorado DRACH model
m6A/A site ratio (%)
DMSO STM2457
81,012 m6A sites
72,047 m6A sites
72,372 m6A sites
C
GLORI (all motifs)
GLORI (DRACH motifs)
140,934 m6A sites
27,926 m6A sites
D
m6A/A site ratio ≥ 10%
Overlapping with Dorado 13,614 (48.8% of GLORI)
m6A/A site ratio ≥ 20%
Overlapping with Dorado 11,536 (69.5% of GLORI)
m6A/A site ratio ≥ 50%
Overlapping with Dorado 6,307 (89.6% of GLORI)
m6A/A site ratio ≥ 80%
Overlapping with Dorado 3,119 (93.7% of GLORI)
E
SPEN m6A sites (genomic alignment)
5.85 mb 15.87 mb 15.89 mb 15.91 mb 15.93 mb
15.86 mb 15.88 mb 15.9 mb 15.92 mb
Dorado
GLORI
Dorado m6A/A (%)
GLORI m6A/A (%)
Dorado GLORI
F
SPEN isoforms with m6A sites (Dorado)
SPEN-201
SPEN-202

Figure 4

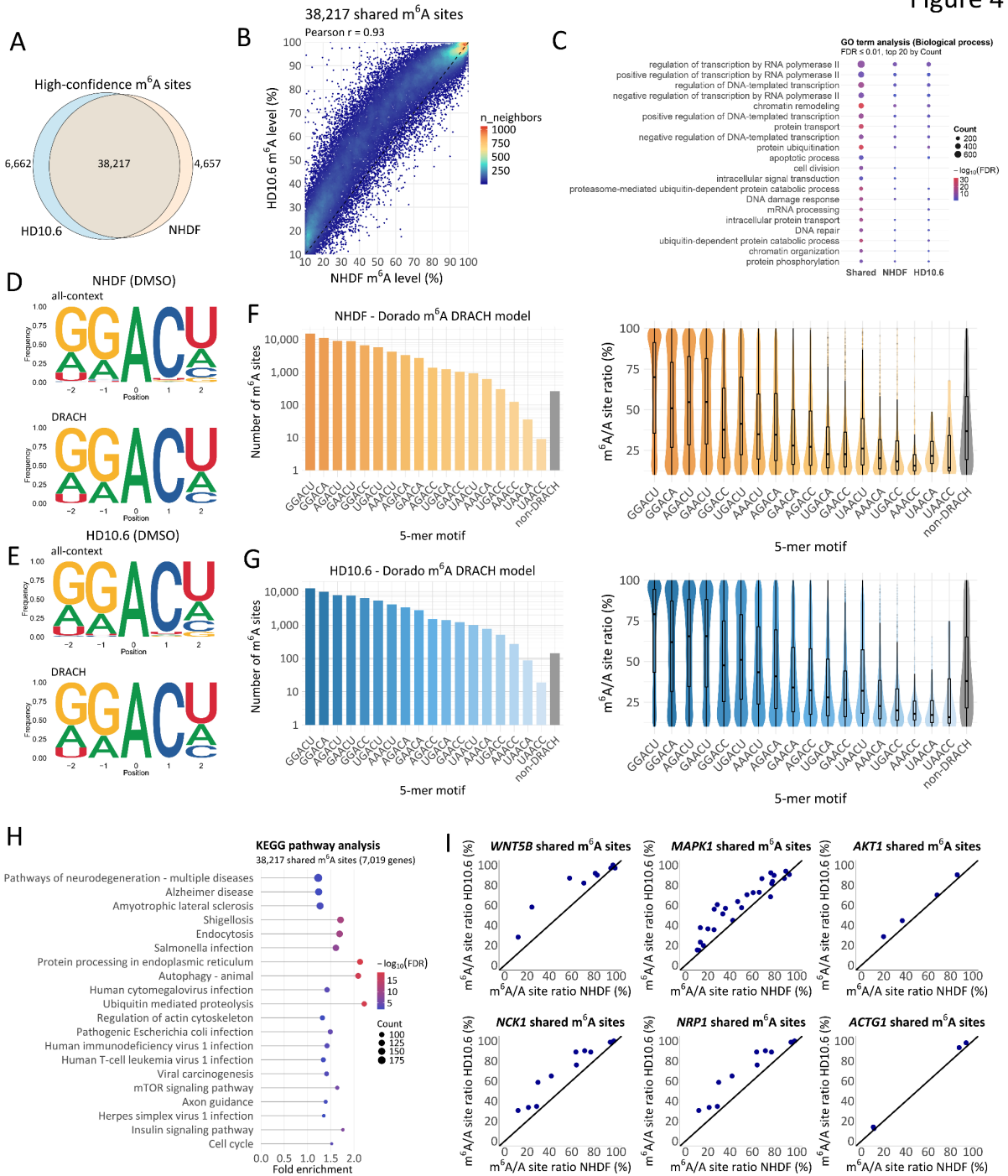
A
High-confidence m6A sites
6,662
38,217
4,657
HD10.6
NHDF
B
38,217 shared m6A sites
Pearson r = 0.93
HD10.6 m6A level (%)
NHDF m6A level (%)
n_neighbors
1000
750
500
250
C
GO term analysis (Biological process)
FDR ≤ 0.01, top 20 by Count
regulation of transcription by RNA polymerase II
positive regulation of transcription by RNA polymerase II
regulation of DNA-templated transcription
negative regulation of transcription by RNA polymerase II
chromatin remodeling
positive regulation of DNA-templated transcription
protein transport
negative regulation of DNA-templated transcription
protein ubiquitination
apoptotic process
cell division
intracellular signal transduction
proteasome-mediated ubiquitin-dependent protein catabolic process
DNA damage response
mRNA processing
intracellular protein transport
DNA repair
ubiquitin-dependent protein catabolic process
chromatin organization
protein phosphorylation
Shared
NHDF
HD10.6
Count
200
400
600
−log10(FDR)
30
20
10
D
NHDF (DMSO)
all-context
DRACH
Frequency
Position
E
HD10.6 (DMSO)
all-context
DRACH
F
NHDF - Dorado m6A DRACH model
Number of m6A sites
5-mer motif
m6A/A site ratio (%)
GGACU
GGACA
AGACU
GAACU
GGACC
UGACU
AAACU
AGACA
GAACA
AGACC
UGACA
GAACC
UAACU
AAACA
UGACC
AAACC
UAACA
UAACC
non-DRACH
G
HD10.6 - Dorado m6A DRACH model
Number of m6A sites
5-mer motif
m6A/A site ratio (%)
H
KEGG pathway analysis
38,217 shared m6A sites (7,019 genes)
Pathways of neurodegeneration - multiple diseases
Alzheimer disease
Amyotrophic lateral sclerosis
Shigellosis
Endocytosis
Salmonella infection
Protein processing in endoplasmic reticulum
Autophagy - animal
Human cytomegalovirus infection
Ubiquitin mediated proteolysis
Regulation of actin cytoskeleton
Pathogenic Escherichia coli infection
Human immunodeficiency virus 1 infection
Human T-cell leukemia virus 1 infection
Viral carcinogenesis
mTOR signaling pathway
Axon guidance
Herpes simplex virus 1 infection
Insulin signaling pathway
Cell cycle
Fold enrichment
−log10(FDR)
15
10
5
Count
100
125
150
175
I
WNT5B shared m6A sites
MAPK1 shared m6A sites
AKT1 shared m6A sites
NCK1 shared m6A sites
NRP1 shared m6A sites
ACTG1 shared m6A sites
m6A/A site ratio HD10.6 (%)
m6A/A site ratio NHDF (%)

Figure S1

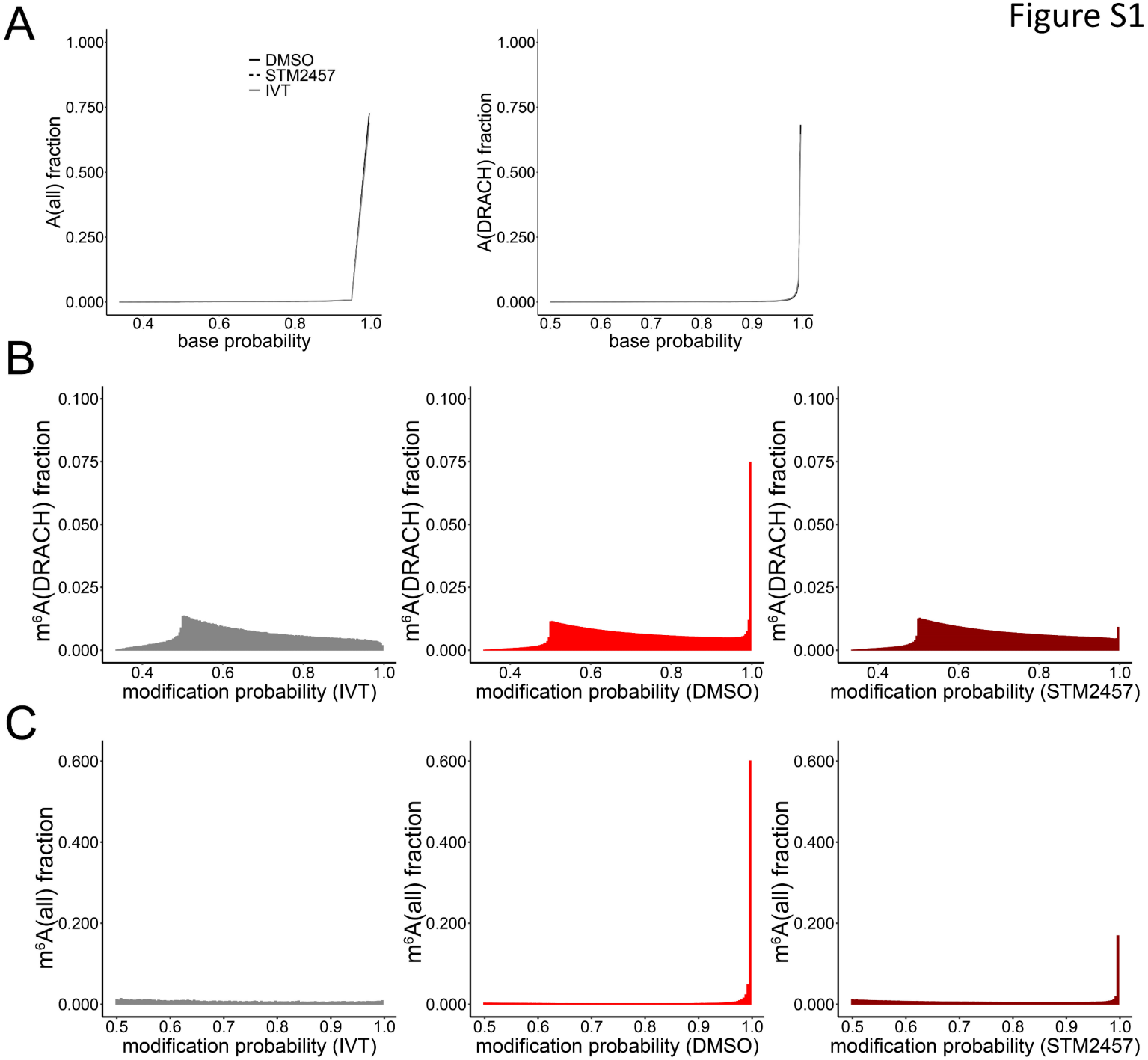
A
DMSO
STM2457
IVT
A(all) fraction
A(DRACH) fraction
base probability
B
m6A(DRACH) fraction
modification probability (IVT)
modification probability (DMSO)
modification probability (STM2457)
C
m6A(all) fraction

Figure S2

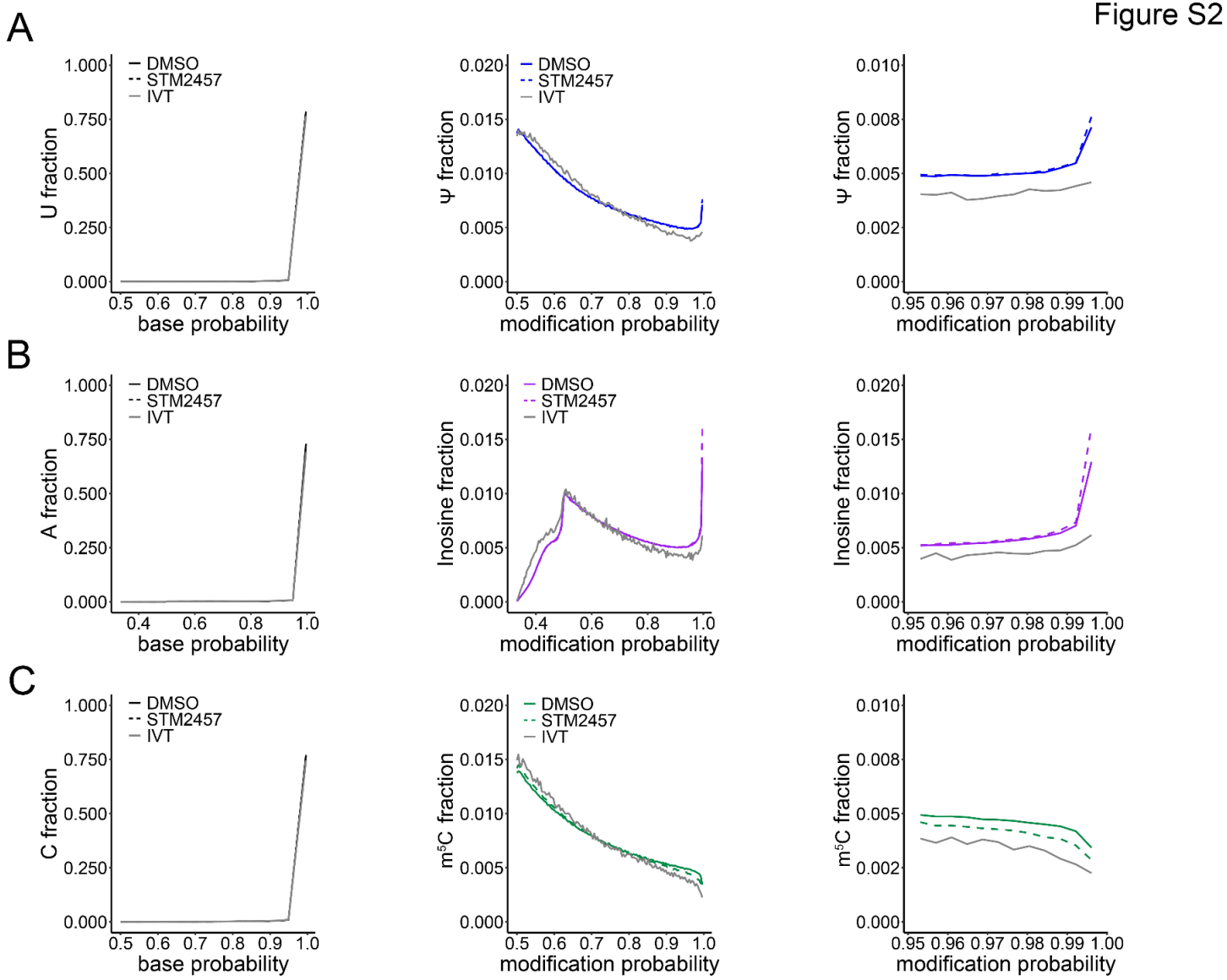
A
DMSO
STM2457
IVT
U fraction
base probability
ψ fraction
modification probability
B
A fraction
Inosine fraction
C
C fraction
m5C fraction

Figure S3

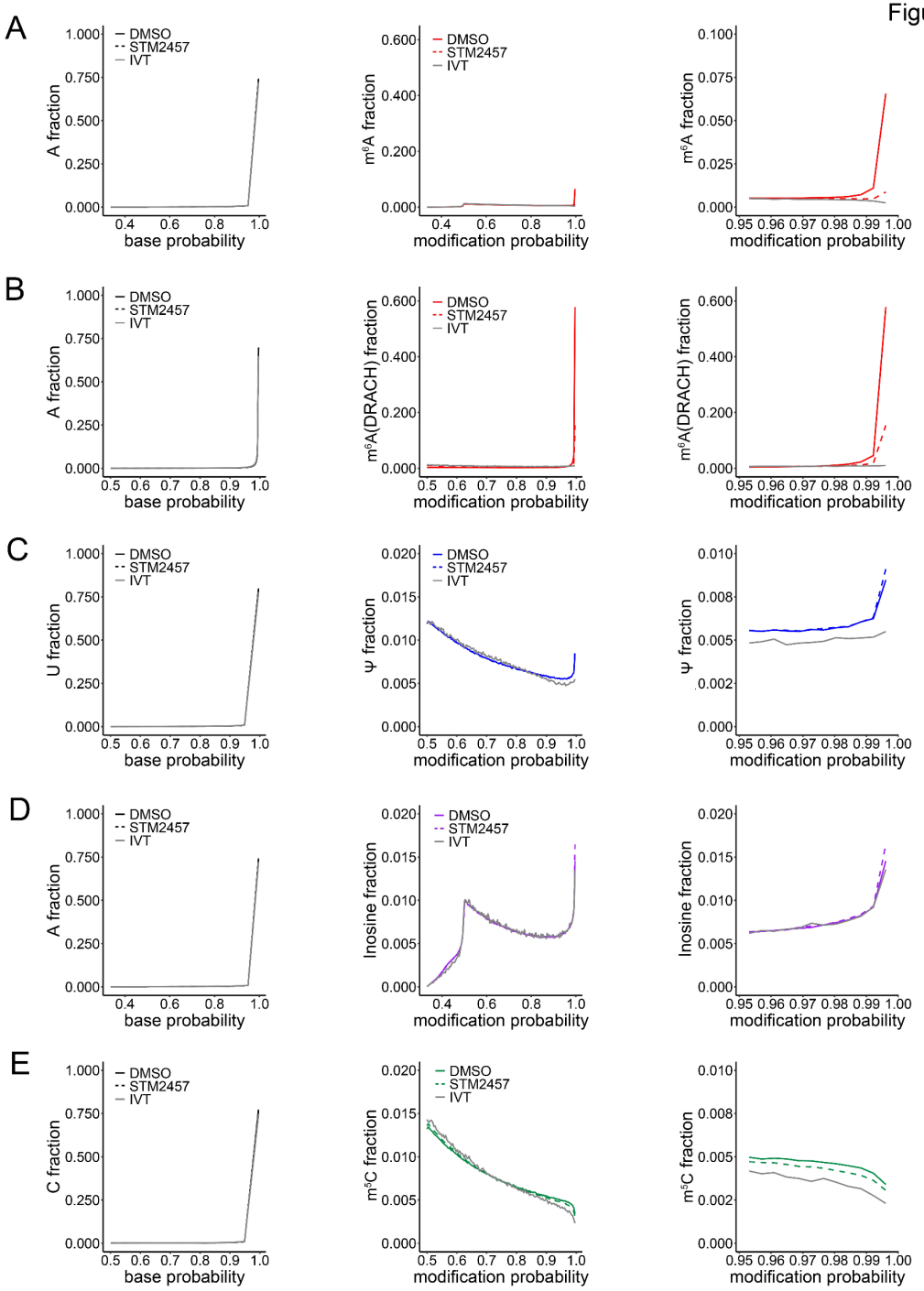
A
DMSO
STM2457
IVT
A fraction
base probability
m6A fraction
modification probability
B
m6A(DRACH) fraction
C
U fraction
Ψ fraction
D
Inosine fraction
E
C fraction
m5C fraction

Figure S4

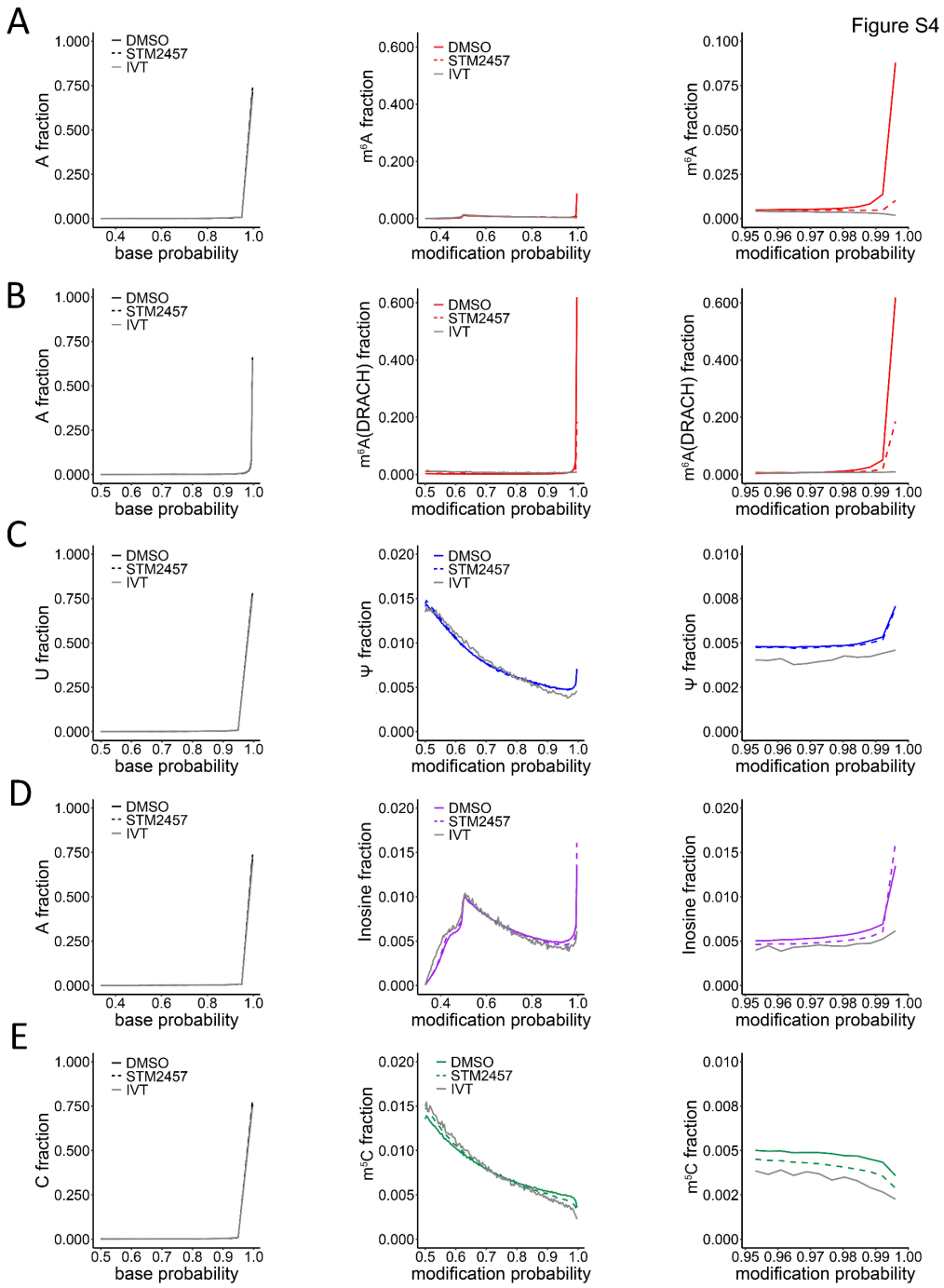
A
B
C
D
E
DMSO
STM2457
IVT
A fraction
m6A fraction
m6A(DRACH) fraction
U fraction
Ψ fraction
Inosine fraction
m5C fraction
C fraction
base probability
modification probability

Figure S5

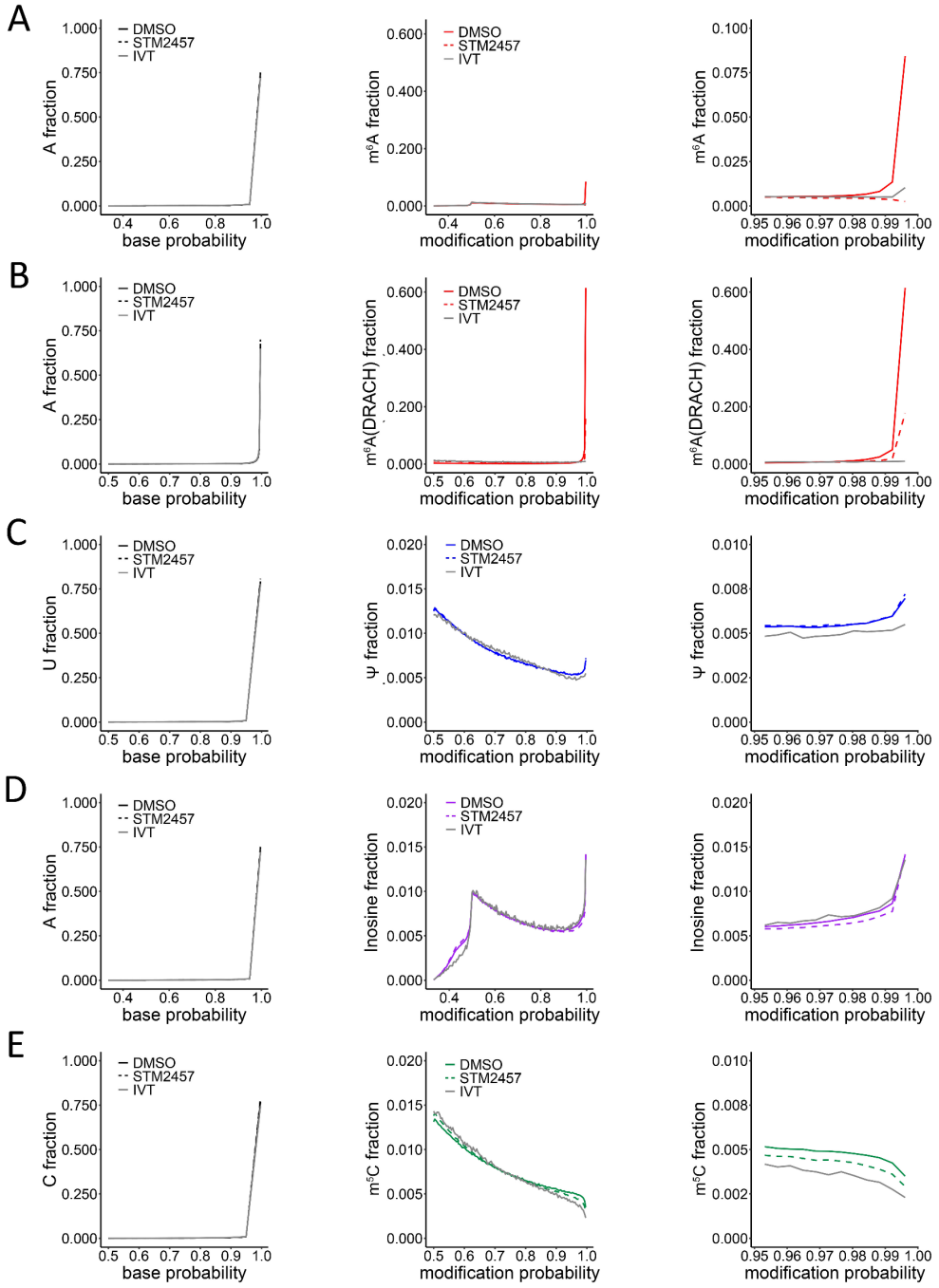
A
B
C
D
E
DMSO
STM2457
IVT
A fraction
m6A fraction
m6A(DRACH) fraction
U fraction
ψ fraction
Inosine fraction
C fraction
m5C fraction
base probability
modification probability

Figure S6

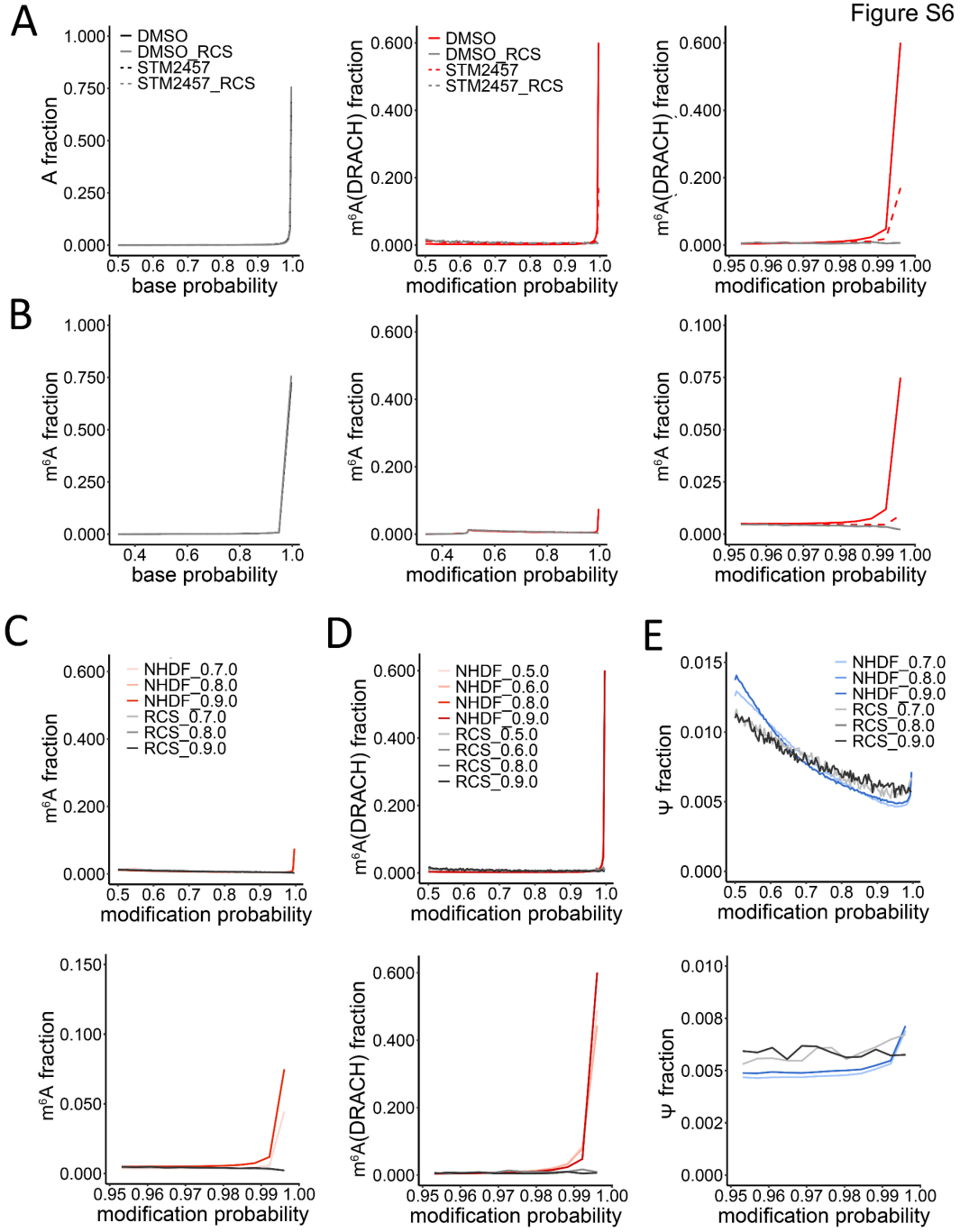
A
DMSO
DMSO_RCS
STM2457
STM2457_RCS
A fraction
base probability
m6A(DRACH) fraction
modification probability
B
m6A fraction
base probability
modification probability
C
NHDF_0.7.0
NHDF_0.8.0
NHDF_0.9.0
RCS_0.7.0
RCS_0.8.0
RCS_0.9.0
D
NHDF_0.5.0
NHDF_0.6.0
NHDF_0.8.0
NHDF_0.9.0
RCS_0.5.0
RCS_0.6.0
RCS_0.8.0
RCS_0.9.0
E
ψ fraction

Figure S7

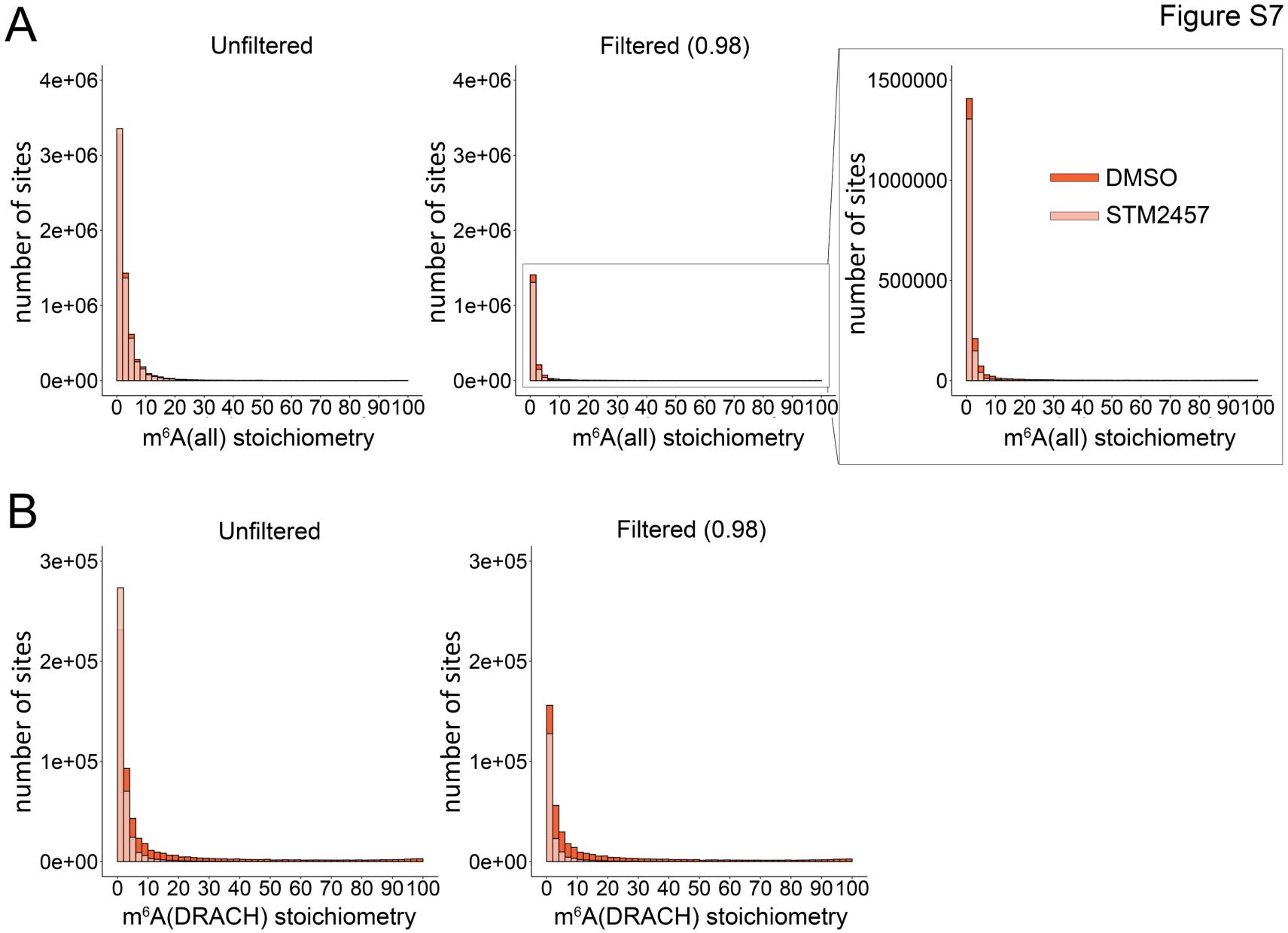
A
Unfiltered
Filtered (0.98)
number of sites
4e+06
3e+06
2e+06
1e+06
0e+00
1500000
1000000
500000
0
0 10 20 30 40 50 60 70 80 90 100
m6A(all) stoichiometry
DMSO
STM2457
B
3e+05
2e+05
1e+05
0e+00
m6A(DRACH) stoichiometry

Figure S8

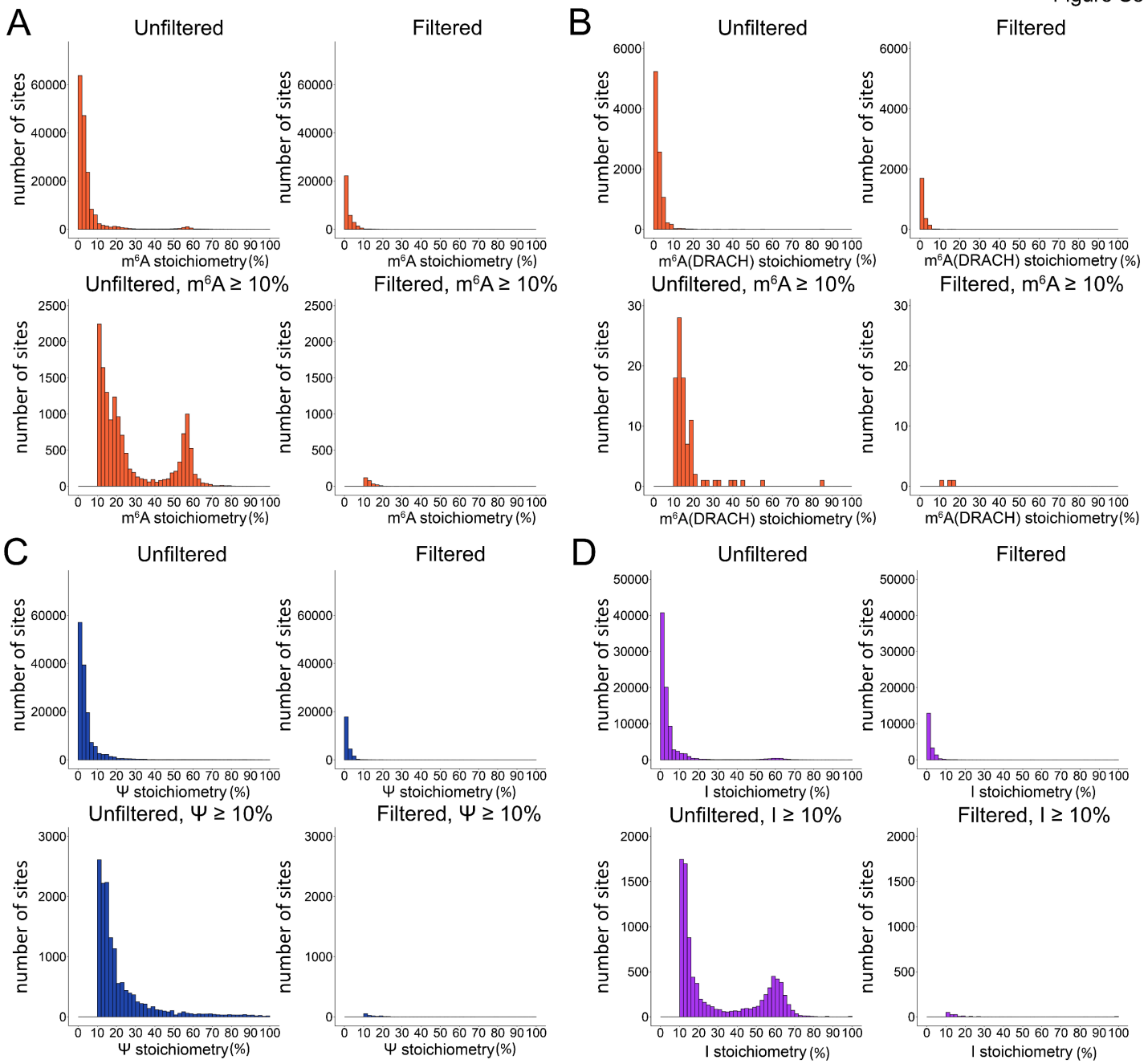
A
Unfiltered
Filtered
number of sites
m6A stoichiometry (%)
Unfiltered, m6A ≥ 10%
Filtered, m6A ≥ 10%
B
m6A(DRACH) stoichiometry (%)
C
Ψ stoichiometry (%)
Unfiltered, Ψ ≥ 10%
Filtered, Ψ ≥ 10%
D
I stoichiometry (%)
Unfiltered, I ≥ 10%
Filtered, I ≥ 10%

Figure S9

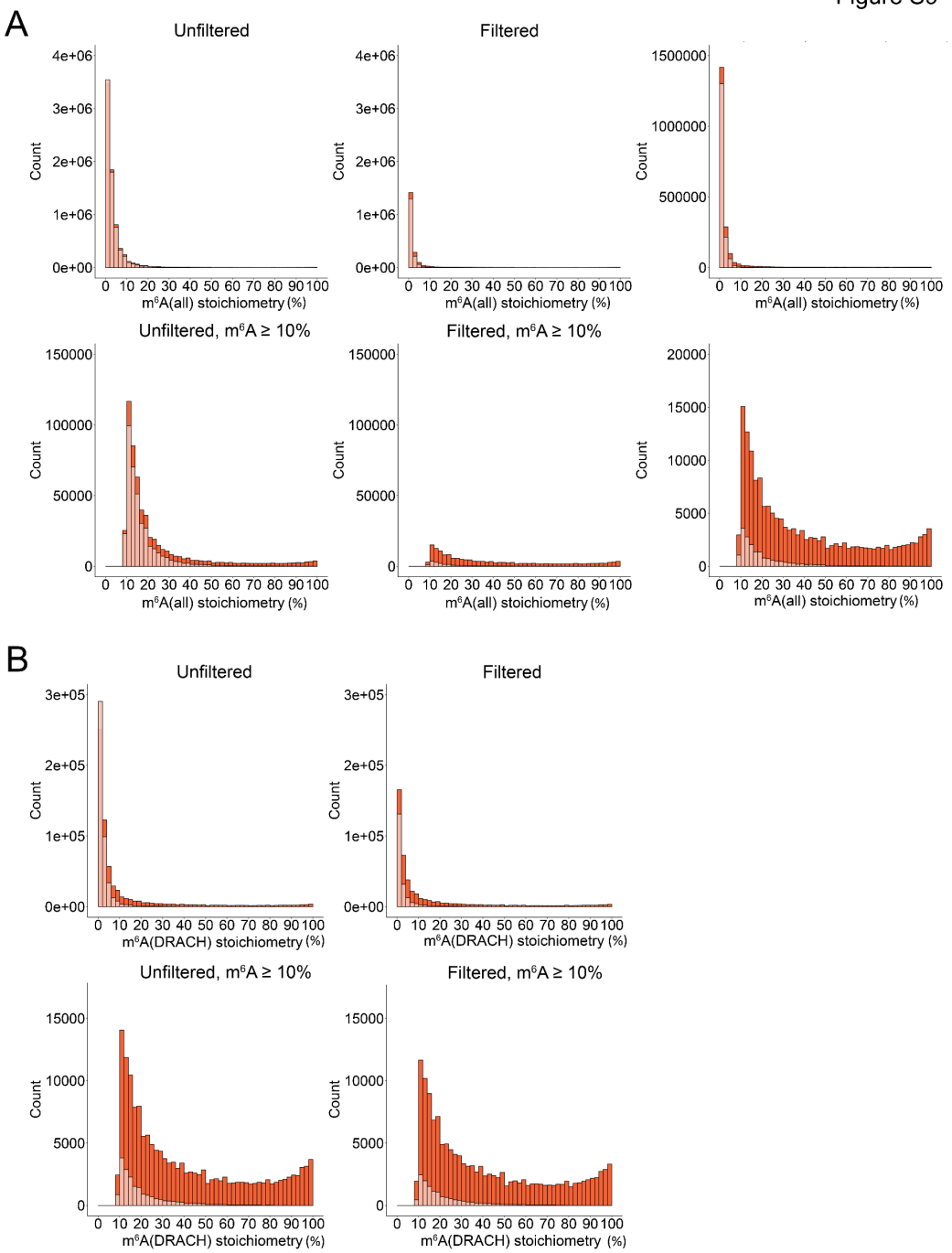
A
Unfiltered
Filtered
Count
m6A(all) stoichiometry (%)
Unfiltered, m6A ≥ 10%
Filtered, m6A ≥ 10%
B
m6A(DRACH) stoichiometry (%)

Figure S10

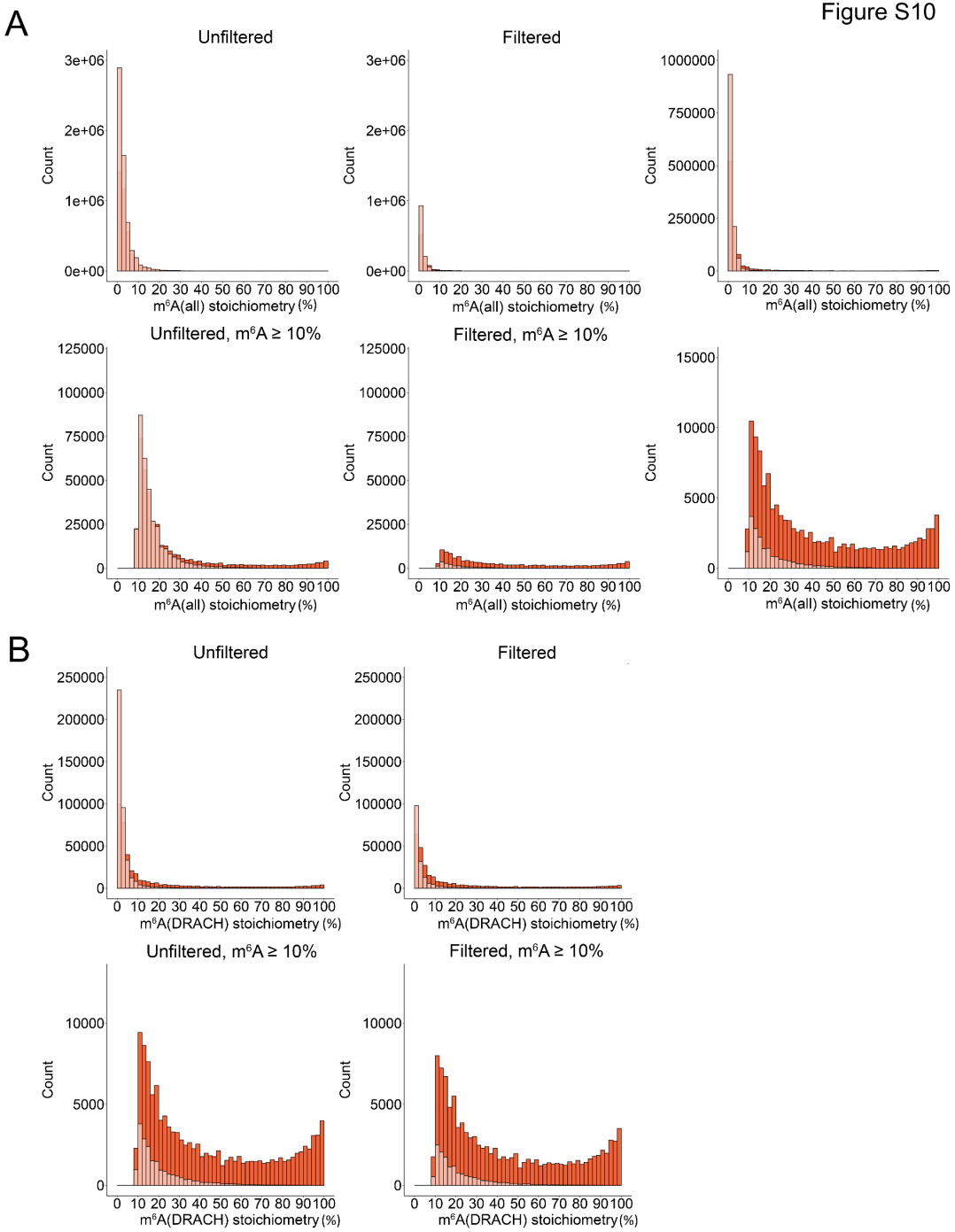
A
Unfiltered
Filtered
Count
m6A(all) stoichiometry (%)
Unfiltered, m6A ≥ 10%
Filtered, m6A ≥ 10%
B
m6A(DRACH) stoichiometry (%)

Figure S11

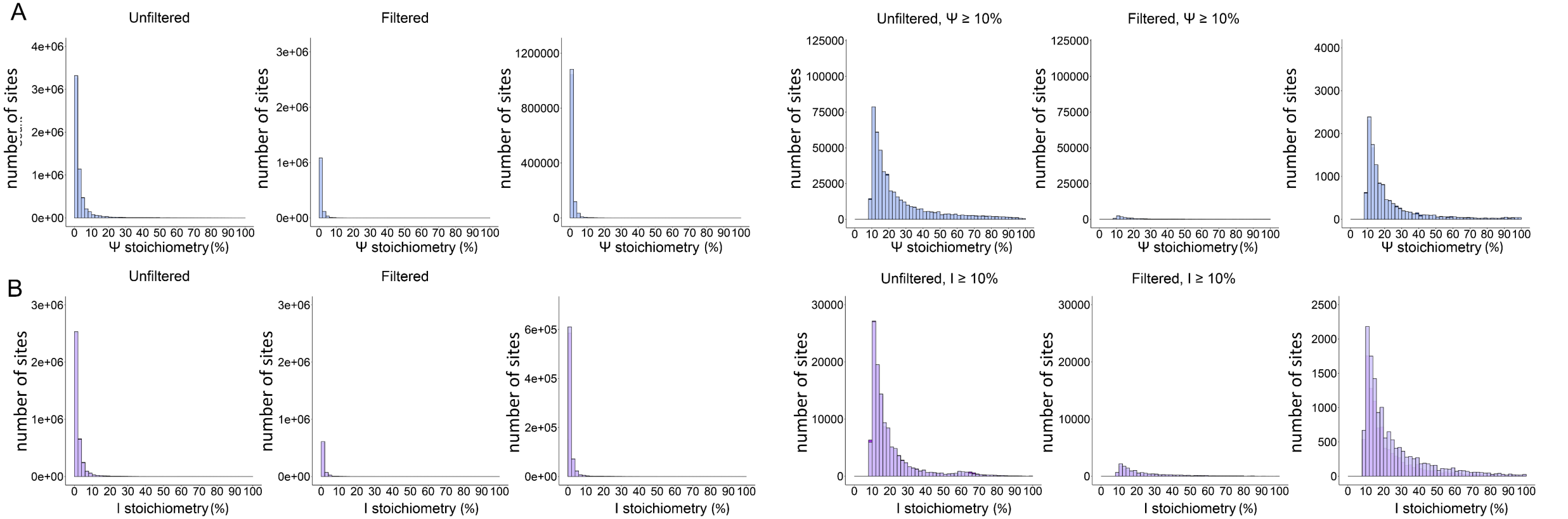
A
Unfiltered
Filtered
Unfiltered, Ψ ≥ 10%
Filtered, Ψ ≥ 10%
number of sites
Ψ stoichiometry (%)
B
Unfiltered
Filtered
Unfiltered, I ≥ 10%
Filtered, I ≥ 10%
number of sites
I stoichiometry (%)

Figure S12

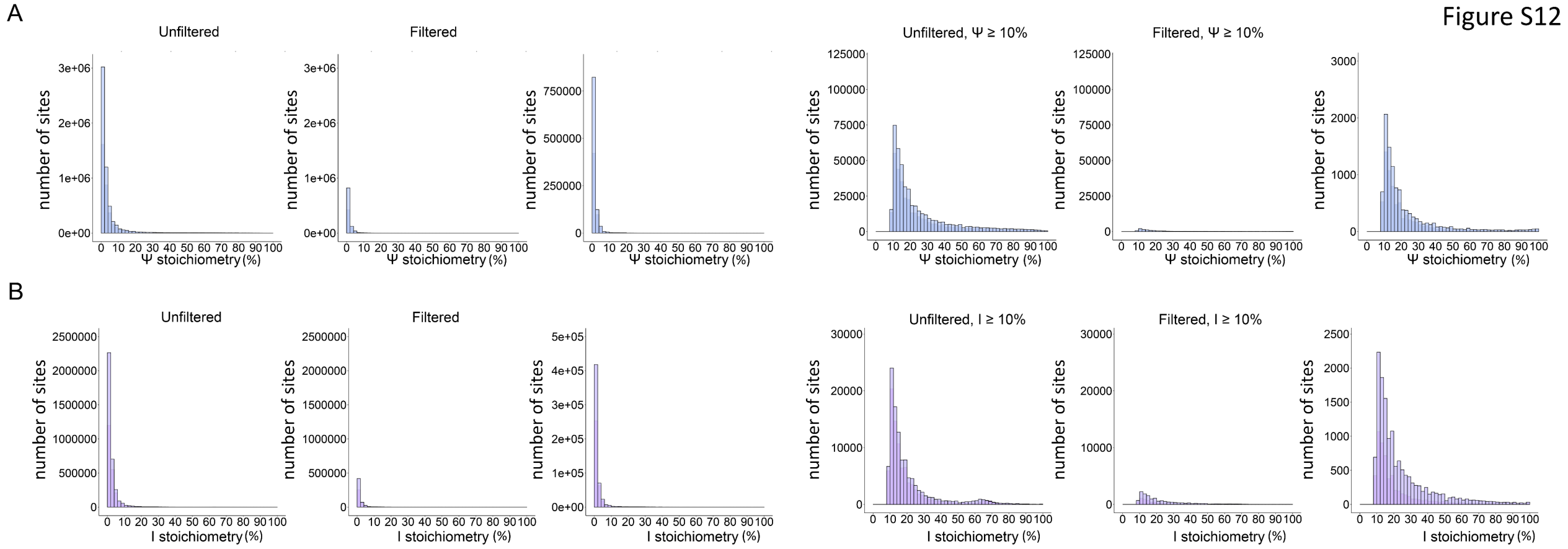
A
Unfiltered
Filtered
Unfiltered, Ψ ≥ 10%
Filtered, Ψ ≥ 10%
number of sites
Ψ stoichiometry (%)
B
Unfiltered
Filtered
Unfiltered, I ≥ 10%
Filtered, I ≥ 10%
number of sites
I stoichiometry (%)

Figure S13

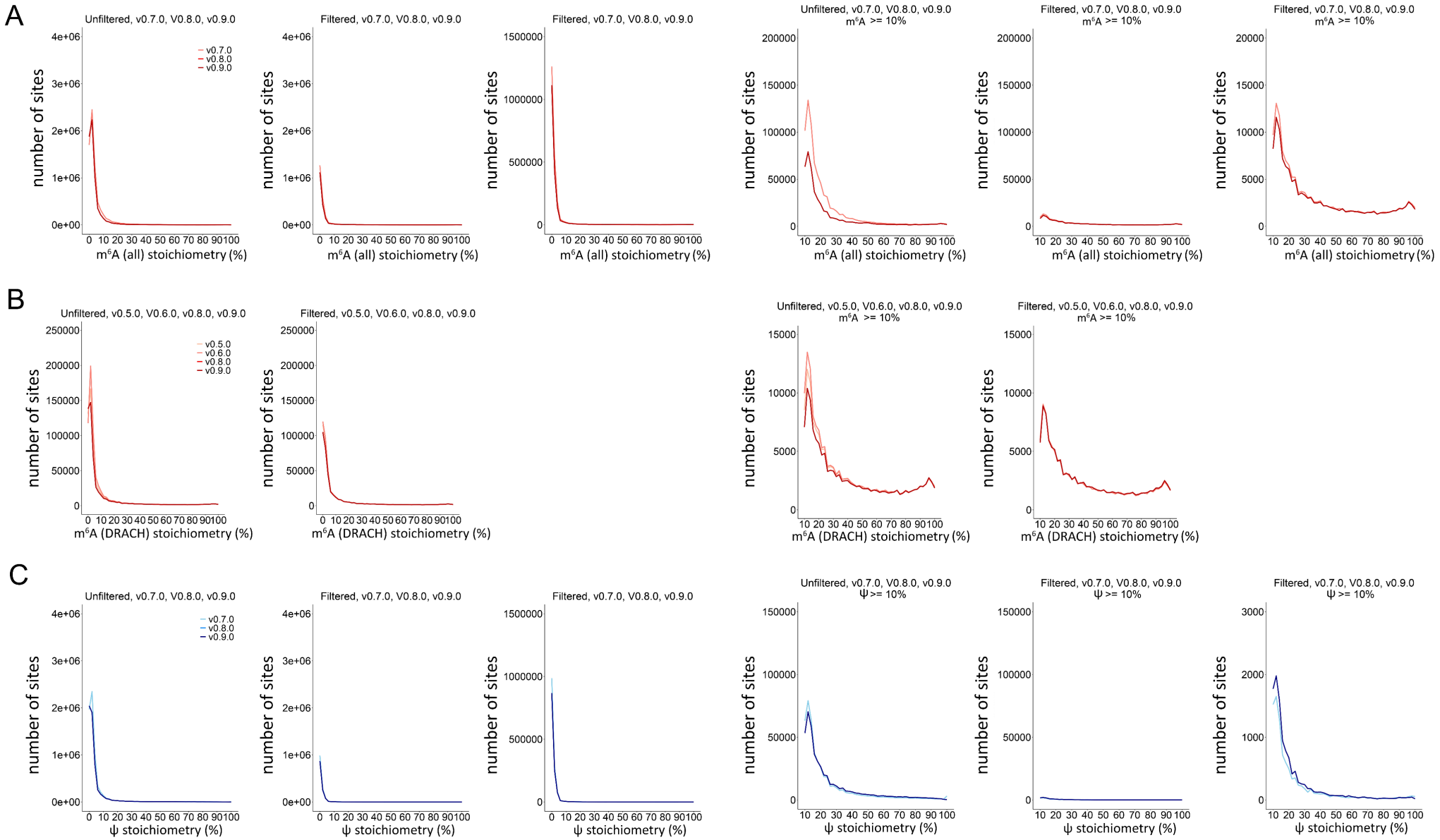
A
Unfiltered, v0.7.0, V0.8.0, v0.9.0
Filtered, v0.7.0, V0.8.0, v0.9.0
Unfiltered, v0.7.0, V0.8.0, v0.9.0
m6A >= 10%
Filtered, v0.7.0, V0.8.0, v0.9.0
m6A >= 10%
v0.7.0
v0.8.0
v0.9.0
number of sites
m6A (all) stoichiometry (%)
B
Unfiltered, v0.5.0, V0.6.0, v0.8.0, v0.9.0
Filtered, v0.5.0, V0.6.0, v0.8.0, v0.9.0
Unfiltered, v0.5.0, V0.6.0, v0.8.0, v0.9.0
m6A >= 10%
Filtered, v0.5.0, V0.6.0, v0.8.0, v0.9.0
m6A >= 10%
v0.5.0
v0.6.0
v0.8.0
v0.9.0
number of sites
m6A (DRACH) stoichiometry (%)
C
Unfiltered, v0.7.0, V0.8.0, v0.9.0
Filtered, v0.7.0, V0.8.0, v0.9.0
Unfiltered, v0.7.0, V0.8.0, v0.9.0
ψ >= 10%
Filtered, v0.7.0, V0.8.0, v0.9.0
ψ >= 10%
v0.7.0
v0.8.0
v0.9.0
number of sites
ψ stoichiometry (%)

Figure S14

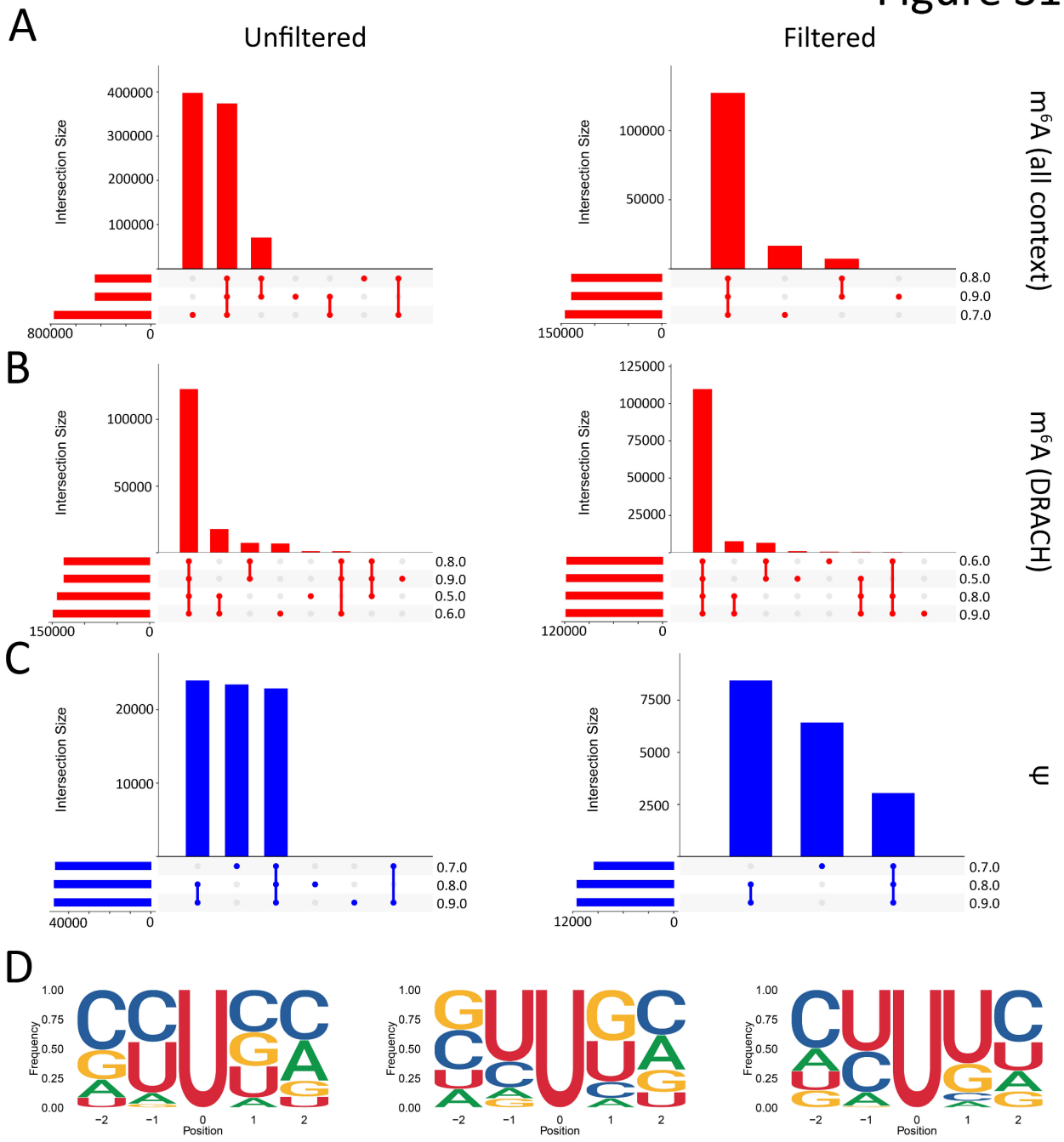
A
Unfiltered
Filtered
Intersection Size
400000
300000
200000
100000
800000
0
100000
50000
150000
0.8.0
0.9.0
0.7.0
m6A (all context)
B
100000
50000
150000
0.8.0
0.9.0
0.5.0
0.6.0
125000
100000
75000
50000
25000
120000
0.6.0
0.5.0
0.8.0
0.9.0
m6A (DRACH)
C
20000
10000
40000
0.7.0
0.8.0
0.9.0
7500
5000
2500
12000
Ψ
D
Frequency
1.00
0.75
0.50
0.25
0.00
−2
−1
0
1
2
Position

Figure S15

A

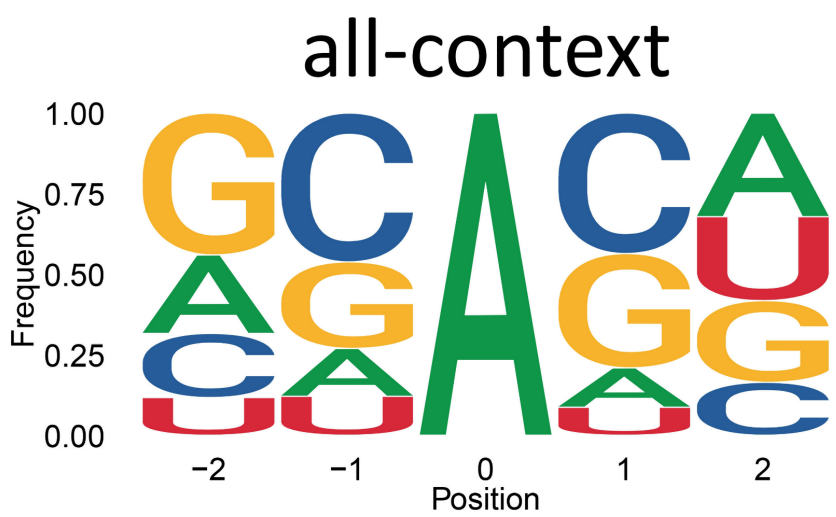

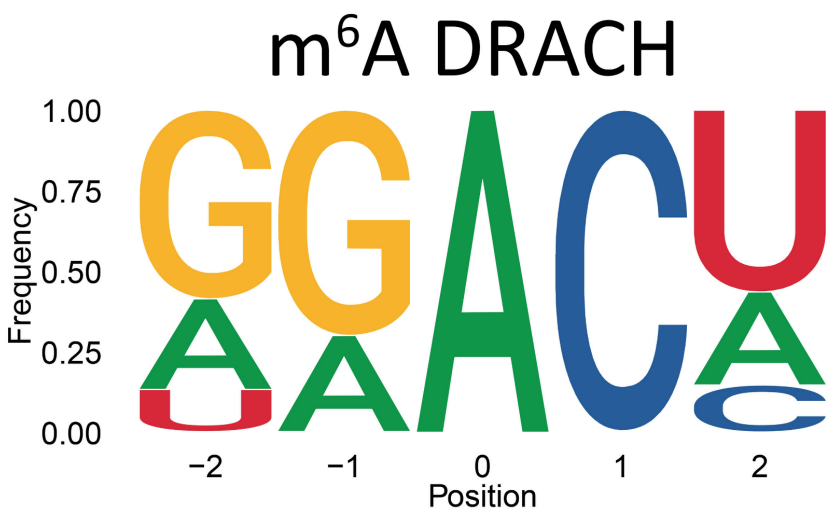

NHDF

B

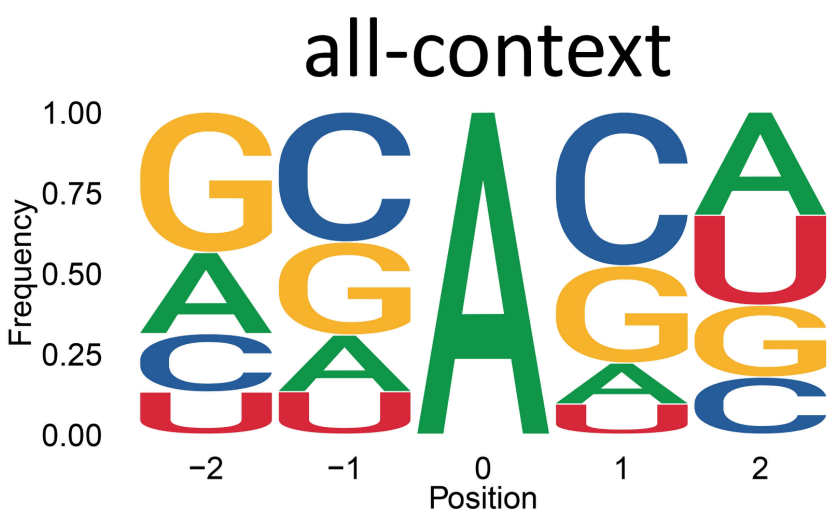

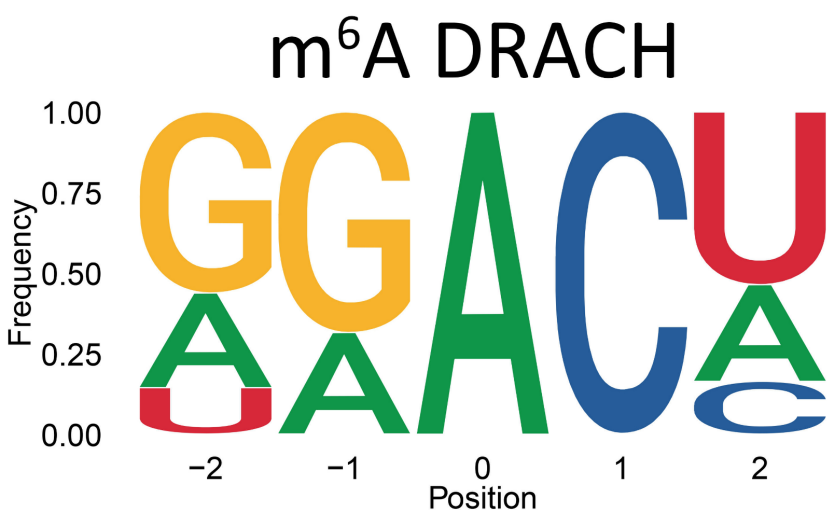

HD10.6

Figure S16

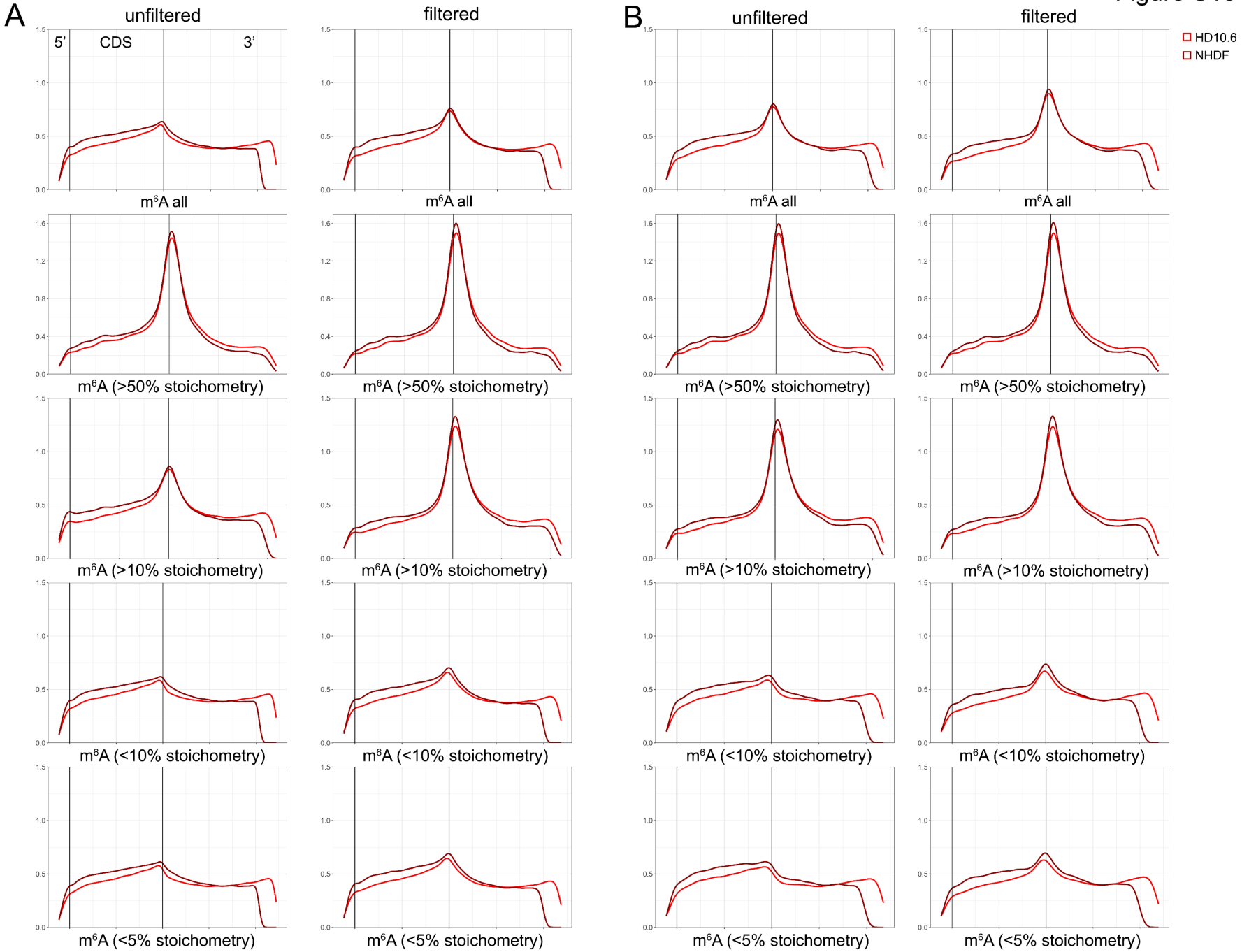
A
unfiltered
filtered
5'
CDS
3'
B
unfiltered
filtered
HD10.6
NHDF
m6A all
m6A (>50% stoichometry)
m6A (>10% stoichometry)
m6A (<10% stoichometry)
m6A (<5% stoichometry)

Figure S17

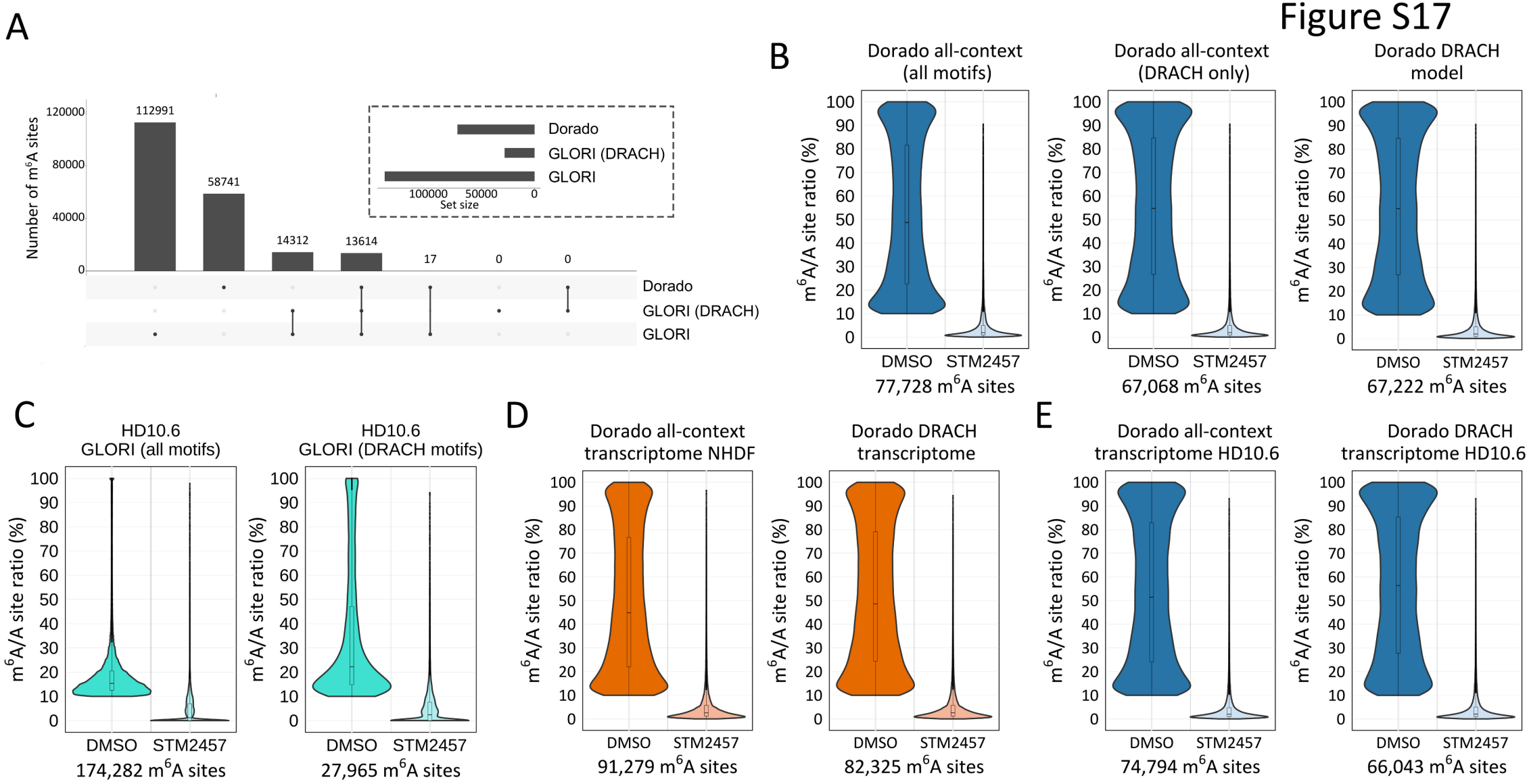
A
Number of m6A sites
120000
80000
40000
0
112991
58741
14312
13614
17
0
0
Dorado
GLORI (DRACH)
GLORI
100000
50000
0
Set size
B
Dorado all-context (all motifs)
Dorado all-context (DRACH only)
Dorado DRACH model
m6A/A site ratio (%)
DMSO
STM2457
77,728 m6A sites
67,068 m6A sites
67,222 m6A sites
C
HD10.6 GLORI (all motifs)
HD10.6 GLORI (DRACH motifs)
174,282 m6A sites
27,965 m6A sites
D
Dorado all-context transcriptome NHDF
Dorado DRACH transcriptome
91,279 m6A sites
82,325 m6A sites
E
Dorado all-context transcriptome HD10.6
Dorado DRACH transcriptome HD10.6
74,794 m6A sites
66,043 m6A sites